

Chapter 7

Feasibility Study for 3D Online Motion Compensation

The current section presents the results of the experimental study of the feasibility of three-dimensional motion online compensation (3D-OMC) for the irradiation of moving target volumes. First, rescanning is investigated experimentally with respect to ion beam irradiation (cf. chapter 7.1). Next, motion compensation is studied for the two orthogonal motion components, lateral in chapter 7.2 and longitudinal in chapter 7.3. Finally, the lateral motion compensation feasibility is shown for complex, extended target volumes in chapter 7.4.

7.1 Rescanning the Target Volume

From the statistical point of view, averaging out motion-related effects on the dose distribution by scanning the same field several times (rescanning, cf. chapter 3.4.1) is a logical approach. It does neither require any technical modification of the beam delivery system, nor major changes in the treatment planning strategy. A detailed, analytical investigation of the rescanning strategy is difficult for active scanning methods, where the dose distribution depends on two superimposed patterns, scanning and target motion [Phi92]. Up to now, no experimental data of the rescanning effect exist for heavy ions beams. To evaluate the feasibility for the irradiation of moving target volumes, the effect of rescanning on intensity modulated heavy ion irradiation was studied with a simple target configuration.

7.1.1 Experimental Setup

A planar film holder was attached 13.5 ± 0.5 mm off centre to a continuously rotating stepping motor¹. Mounted on an axis, the holder remained its orientation in the room while the motor was rotating.

¹Continuously means, that there is no restriction in the number of rotations. After a full rotation, the motor is *exactly* in the same state as before.

The excentric mounting transformed the motor rotation into a superposition of periodical translations in x and y direction with an amplitude of ± 13.5 mm and a phase difference of $\frac{\pi}{2}$. The rotation frequency of the motor was set to 3.5 ± 0.5 s to reflect respiration-related target motion in 2D.

X-ray films were placed on the holder. During motion the films were irradiated with a squared field with a constant number of ions ($E=153.66 \frac{\text{MeV}}{\text{u}}$, FWHM=6.5 mm). The resulting dose distribution has a flat top (homogeneous) and a sharp, but finite dose fall-off at the border of the field. If the target moves during the irradiation the region of dose fall-off is smeared over a distance equal to the motion amplitude, reducing the dose homogeneity. To deposit a homogeneous dose with the rescanning technique in the moving target area, the size of the irradiation field has to be increased by at least the size of the motion amplitude to account for the smeared dose fall-off. For the experimental study of rescanning, a $120 \times 120 \text{ mm}^2$ irradiation field was chosen to fill a $90 \times 90 \text{ mm}^2$ square, which moved by ± 13.5 mm, homogeneously with dose.

To investigate the rescanning effect, the dose was applied to the films in a different number of scans. The number of particles per point was scaled according to the number of repeated exposures. The start of irradiation was not correlated to the target motion. For each film the repeated scans were applied directly after each other without interruption of the target motion. Experiments for rescanning 2, 3, 5 and 10 times are presented. In case of 2, 3 and 5 times scanning, the complete irradiation process lasted approximately 2-3 min per film. Due to a reduced beam intensity, scanning the target 10 times lasted approximately twice as long. After irradiation, reference marks were added to the films in order to determine the exact position of the isocentre in the off-line data analysis. Moreover, a calibration curve was recorded on a separate film to extract the value for the saturation optical density $optD_{max}$. Each experiment was performed five times.

7.1.2 Data Analysis

The film detector signals of the 2D irradiation field were first prepared by subtracting the background contribution from the measured optical density². All films of the rescanning experiment showed a background of 0.24. The resulting (net-) optical density was normalised to the maximum optical density, which was determined to be $optD_{max}=3.5$. All dose distributions were shifted to a common isocentre, defining the position of the region of interest (ROI), according to reference marks on the films. The optical density was converted to dose using eq. (6.3) with a film response $m=0.34 \text{ Gy}^{-1}$ for $E=150 \frac{\text{MeV}}{\text{u}}$ [Bat00].

The dose homogeneity H_d of the irradiation field was calculated for different regions of interest from the dose distributions according to eq. (4.1). In addition, the frac-

²The amount of background was determined from cuts on the non-irradiated regions of the film.

tion of total dose deposited outside of the $90 \times 90 \text{ mm}^2$ target area was determined and compared to the fraction outside of the planned $120 \times 120 \text{ mm}^2$ irradiation field.

7.1.3 Results and Discussion

Fig. 7.1 shows the 2D optical density distribution delivered to a static target compared to those to moving targets with different number of scans. Scanning a moving

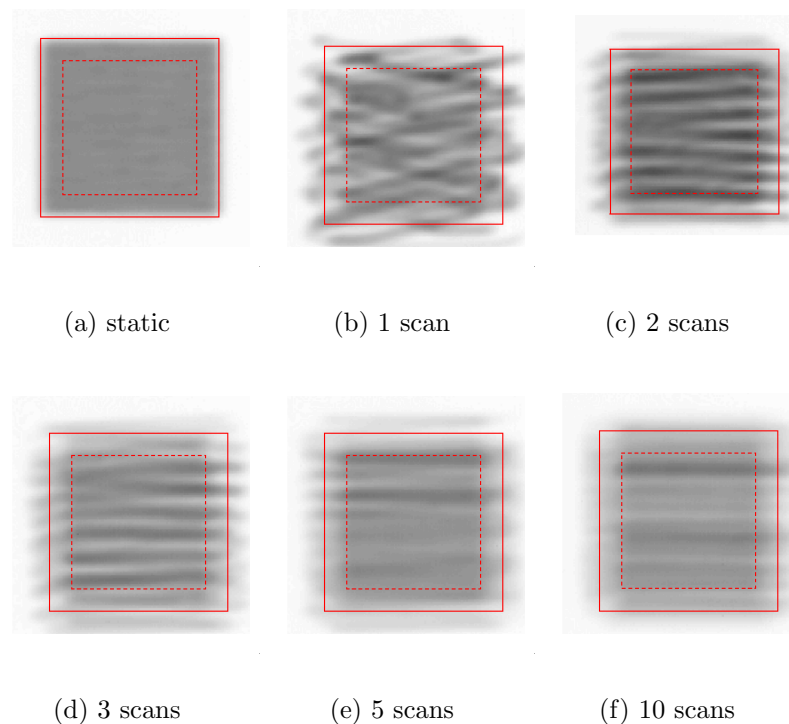


Figure 7.1:

Examples of the measured dose distribution of a $120 \times 120 \text{ mm}^2$ square for different rescanning conditions. The field was irradiated on a moving target with different number of scans. The particle fluence was in each case adapted to yield a constant, integral dose over all scans. The static case was taken as reference. The solid line indicates the size of the planned irradiation field and the dashed line the actual target area.

target once leads to a completely inhomogeneous film signal, that means that the dose distribution is heavily distorted. A lot of hot and cold spots are visible in the irradiated field (solid line). Moreover, parts outside the planned irradiation field received a dose of the same order than the average dose inside. In a clinical case, these parts would contain normal tissue which was not planned to receive the full

therapeutic dose. Scanning the moving target several times with a reduced dose, the dose distribution is visibly improved, especially inside the target area (dashed line). The cold and hot spots are smeared, resulting in lines of under- and overdosage. The transition from spots to lines can be explained by the time correlation between scanning and target motion. If the target is for instance scanned five times in the same time as one scan, the single scans are five times as fast (the reduced dose leads to a lower particle deposition and consequently to a higher scanning speed). While in the case of a single scan the target moves significantly during the irradiation of one point, a couple of consecutive points can be irradiated in the same time in case of five scans. As the scanner proceeds in horizontal lines, staggered stripes appear in the final dose distribution. Compared to 1-3 scans, the 5 and 10 times rescanned dose distributions show significantly less dominant line structures, but the dose is still smeared at the borders of the irradiation field. Due to the double dynamical nature of rescanning a moving target with a dynamic beam delivery system, a detailed analysis is difficult. For a single scan, the interplay between scanning and target motion generates discrete dose delocalisation patterns. The detailed pattern depends on the time correlation between the two motions. If the field is scanned multiple times with uncorrelated initial phases, different dose patterns are superimposed, which leads to a certain averaging over the inhomogeneities.

Since rescanning is a statistical process, the experiment was repeated five times. The complete set of 25 films is shown in fig. 7.2. Apart from the improvement in homogeneity the growing variety in the dose distributions with increasing number of scans can clearly be observed. As expected from the calculations in chapter 4.3.4 the amount of different dose distributions increases with the number of scans. The three right-hand image for 10 times scanning show impressively how an unfavourable interplay between scanning and target motion creates strong distortions, which even decrease the homogeneity again. The large differences between the left- and right-hand image of 10 times scanning, for instance, show that in a double dynamical system certain phase combinations exist which eliminate the averaging effect of a higher number of scans³.

Due to purely statistical considerations, the dose inhomogeneity ($1-H_d$) is expected to decrease with $\frac{1}{\sqrt{n}}$, where n is the number of scans [Bor02]. Fig. 7.3 shows the dose inhomogeneity over differently sized ROIs centred in the $120 \times 120 \text{ mm}^2$ irradiation field. The dose homogeneity is averaged over five measurements under the same conditions and the error bars correspond to the statistical standard deviation. A fit to the data points shows a good agreement with the expected $\frac{1}{\sqrt{n}}$ dependence. A significant deviation due to a change in irradiation conditions is observed for the case of 10 times scanning. At GSI, the parameters for the beam delivery system

³The interference pattern of the 10 times scanning case differs significantly from the other four cases, since the irradiation was based on a different time correlation (discussed below), which however remained constant for all five measurements with 10 times rescanning.

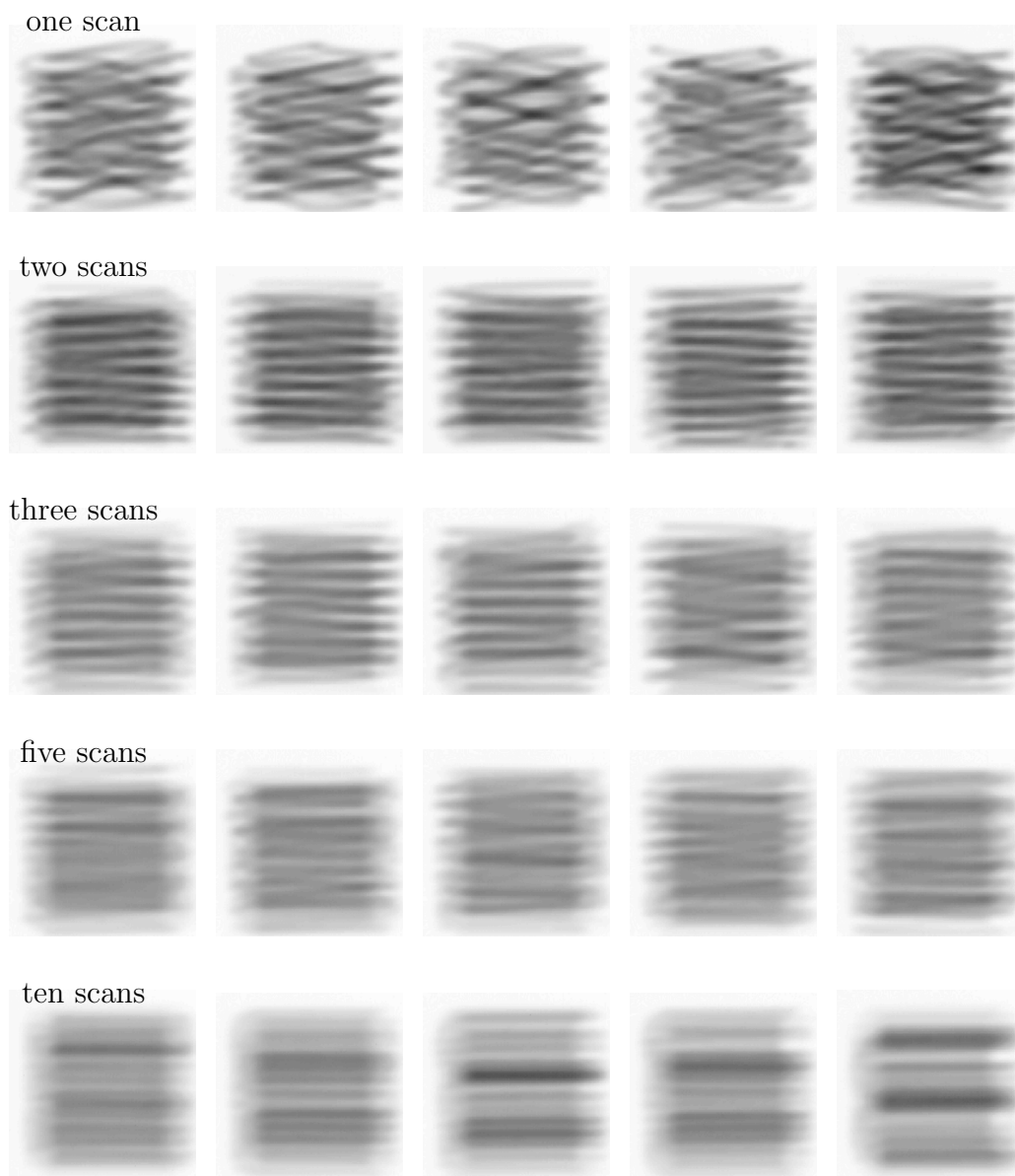


Figure 7.2:

Measured 2D film signal for the rescanning experiment. The complete set of film images is shown irradiated with different number of scans but with the same integral dose in the presence of respiration-like target motion. The number of scans increases from top to bottom. For each number of scans five independent measurements are shown in one row. Brightness and contrast are manually adapted for improved visibility.

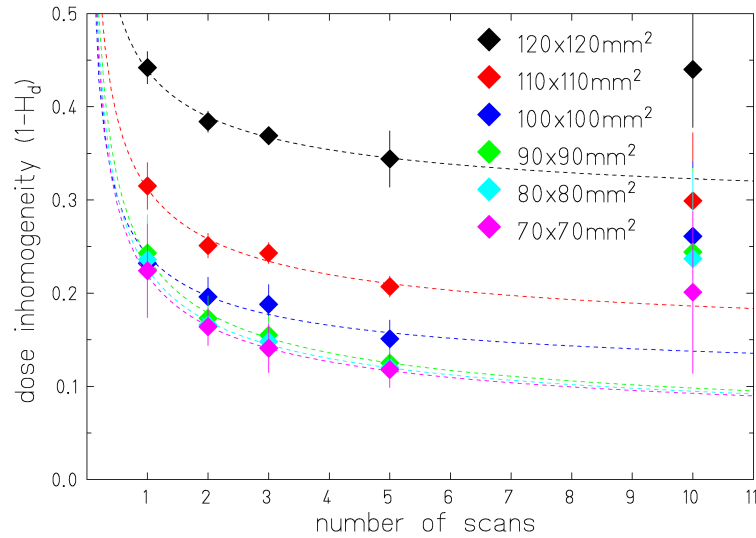


Figure 7.3:

Dose inhomogeneity inside a ROI of different size. For each number of scans, the value is averaged over 5 independent measurements under the same conditions.

are optimised with respect to the dose rate. When changing the dose of the single plans over a large range the system automatically adapts the beam intensity level for the irradiation. In the current experiment a 10 times reduced single plan dose leads to a lower beam intensity than used in the other four cases. Having been irradiated under different conditions (modified time correlation between scanning and target motion), a comparison between the 10 times scanned case and the other four is not possible. Thus, this data point was excluded from the fit.

In the limit of infinite scans, the target motion is described by a spatial probability density, which has to be folded with the dose distribution of the static case. With increasing number of scans the dose inhomogeneity plotted in fig. 7.3 approaches a constant value, which is, due to differences in the spatial probability density, close to but not identical with the dose inhomogeneity in the static case. The homogeneity limit for an infinite number of scans (H_d^{limit}) was extracted from the fit parameters. As discussed in chapter 7.1.1 the calculated dose homogeneity depends on the contribution of partial volumes with a reduced dose from the dose fall-off region. Tab. 7.1 shows the influence of the ROI size on the dose homogeneity of the static target (H_d^{static}) compared to the homogeneity limit for an infinite number of scans (H_d^{limit}). The influence of the fall-off region on the static dose distribution is almost eliminated reducing the ROI size by ± 5 mm in each direction. This is consistent with the prediction of dose distribution from treatment planning. If required the dose fall-off region can be shifted further out of the target volume in the treatment planning process, increasing the dose homogeneity inside the target

| ROI size | $(1 - H_d^{limit})$ | $(1 - H_d^{static})$ | $(1 - H_d^{limit}) / (1 - H_d^{static})$ |
|-------------------------------|---------------------|----------------------|--|
| $120 \times 120 \text{ mm}^2$ | 0.269 ± 0.029 | 0.187 | 1.4 |
| $110 \times 110 \text{ mm}^2$ | 0.128 ± 0.027 | 0.039 | 3.3 |
| $100 \times 100 \text{ mm}^2$ | 0.090 ± 0.049 | 0.020 | 2.2 |
| $90 \times 90 \text{ mm}^2$ | 0.033 ± 0.038 | 0.020 | 1.7 |
| $80 \times 80 \text{ mm}^2$ | 0.034 ± 0.043 | 0.021 | 1.6 |
| $70 \times 70 \text{ mm}^2$ | 0.034 ± 0.049 | 0.021 | 1.6 |

Table 7.1:

Limits of dose inhomogeneity for an infinite number of scans ($1 - H_d^{limit}$) compared to the inhomogeneity of the static distribution ($1 - H_d^{static}$) in dependence of the ROI size. The irradiation field had a size of $120 \times 120 \text{ mm}^2$ and the motion amplitude was $\pm 15 \text{ mm}$ in x and y direction. A beam diameter of FWHM=6.5 mm was used for the irradiation.

volume but also the dose contamination of the surrounding normal tissue. As expected, if the target moves during the irradiation, only the inner $90 \times 90 \text{ mm}^2$ of the irradiation field receive a homogeneous dose distribution. This ROI size corresponds to the size of the irradiation field reduced by the motion amplitude in each direction.

Tab. 7.2 shows the fraction of total dose which was deposited outside of the $90 \times 90 \text{ mm}^2$ target area and the planned $120 \times 120 \text{ mm}^2$ irradiation field for the different measurements. Except for the static case, each of the values is averaged over the five independent measurements. Obviously, the fraction of misplaced dose is

| | fraction of total dose outside the considered ROI | |
|---------|---|-------------------------------|
| | $90 \times 90 \text{ mm}^2$ | $120 \times 120 \text{ mm}^2$ |
| static | 0.153* | 0.028 |
| 1 scan | 0.417 ± 0.007 | 0.130 ± 0.008 |
| 2 scans | 0.414 ± 0.007 | 0.128 ± 0.012 |
| 3 scans | 0.409 ± 0.003 | 0.130 ± 0.010 |
| 5 scans | 0.418 ± 0.009 | 0.129 ± 0.007 |

* calculated for a $90 \times 90 \text{ mm}^2$ irradiation field, since no additional margin is required for a static target

Table 7.2:

Fraction of total dose which is deposited outside the target area ($90 \times 90 \text{ mm}^2$) and the planned irradiation field ($120 \times 120 \text{ mm}^2$) in the rescanning experiment.

for both ROIs independent of the number of scans. According to the study of *Bortfeld et al.* the expectation value for the dose to a single point inside the target area is independent of the number of scans [Bor02]. A re-distribution of

the dose inside the ROI does in average not affect the fraction of misplaced dose outside. In the investigated case, the dose contribution to the outside of the target volume is increased by almost a factor of three when applying a margin required to irradiate the moving target area homogeneously with rescanning. This margin has to be included in treatment planning by considering an increased irradiation field. However, rescanning a moving target even increases the dose deposited outside of the planned irradiation field by more than a factor of three compared to the static case. It has to be emphasised, that these values strongly depend on the detailed shape of the target volume and the conditions of the irradiation. However, the investigated target volume, had a very simple, regular geometry. For more complex shapes the dose contribution to the surrounding area is expected to be even larger. In summary, rescanning improves the dose distribution delivered to a moving target ($\sim \frac{1}{\sqrt{n}}$) over large parts of the irradiation field, although many scans might be required and the final dose distribution depends on the treatment parameters. To extend the homogeneous region to the whole target volume, adequate margins have to be added when using rescanning [Chu03, Yu98, Phi92], increasing the amount of misplaced dose in the normal tissue.

7.2 Lateral Online Motion Compensation

In contrast to the statistical nature of the rescanning approach, online motion compensation is based on a precise compensation of target motion. In the ideal case, no dose is misplaced and the dose distribution is not smeared. Consequently, the dose contribution to the normal tissue is not increased and the dose fall-off is as sharp as for a static target. In reality, the effect on the dose distribution directly depends on the accuracy of beam position correction in each of the three dimensions. In the current section the lateral motion compensation using the magnetic raster scanner is investigated under realistic conditions. The longitudinal compensation with the wedge drive system is studied in chapter 7.3.

7.2.1 Experimental Setup

Lateral target motion was induced with the 3D positioning table (cf. chapter 6.1). X-ray films were attached to a film holder, mounted on the object table. During irradiation the films were moved orthogonal to the beam direction. For each experiment three films were irradiated as follows: a static one as reference, a moving one without motion compensation and a compensated one with 3D-OMC activated. In the compensated case, the displacement of the object table was measured at a fixed frequency by encoders attached to each of the axes.

The positioning table moved periodically with an amplitude of ± 15 mm in both x and y directions. Due to technical reasons, the frequency of this motion was

with 9-12s slower than a typical respiration-related target motion. To smooth the motion pattern, the table was operated in accelerated mode.

To investigate the lateral motion compensation, different patterns were irradiated on the films: The first pattern consisted of five single spots, four at the corners of a $40 \times 40 \text{ mm}^2$ square and one in the centre. These points were irradiated with a fine beam focus setting (nominal: FWHM=4.4 mm) and a beam energy of $246.57 \frac{\text{MeV}}{\text{u}}$. To have a strong motion impact a high particle deposition was chosen, spanning the irradiation of a single spot over more than one spill. To investigate the reproducibility without aligning different films relative to each other, the sequence of the spot irradiation was repeated five times on the same film. If the compensated beam position varied, the width of the measured film profile would increase.

The second pattern consisted of eight parallel lines. Continuous line scans are extremely sensitive to beam displacement orthogonal to the lines. Two different line orientations were used to investigate the compensation accuracy in both lateral directions. A set of horizontal lines was used to probe the vertical compensation accuracy and vice versa. To draw the horizontal lines, the scanner moved according to the standard scanning path algorithm with x as the fast scanning direction. For the vertical line pattern the new algorithm *tm* (cf. chapter 5.2.3) was used, defining y as the fast scanning direction. The lines had a length of 120 mm and were placed 15 mm apart. For this pattern a wider beam of nominal FWHM=6.5 mm and a beam energy of $153.66 \frac{\text{MeV}}{\text{u}}$ were used.

The last pattern consisted of a homogeneously filled square of $120 \times 120 \text{ mm}^2$. This pattern corresponds to the line pattern with filled spacings and is absolutely identical with the pattern used for the rescanning experiments (cf. chapter 7.1). The square was irradiated with the fast scanning direction in x, independent of the orientation of the target motion.

7.2.2 Data Analysis

For all films of the lateral compensation verification, a background of 0.225 was subtracted from the measured optical density. The resulting net optical density was normalised to the maximum optical density, determined to be $optD_{max}=3.5$. The data for all films of the same experiment were shifted to a common isocentre using reference marks on the films.

Due to the strongly non-linear behaviour of the film signal, the resulting optical density distribution does not directly show the effect on the particle distribution. For the spot and the line pattern, the optical density was converted to the corresponding particle fluence F according to eq. (6.3) with the exponent $m \cdot D$ substituted by $\sigma \cdot F$. The activation cross sections σ were taken from [Bat00], $\sigma=0.55 \times 10^{-8} \text{ cm}^2$ for the spot and $0.66 \times 10^{-8} \text{ cm}^2$ for the line pattern. For the homogeneous square, the optical density was converted into dose according to the unmodified eq. (6.3). A film response of $m=0.34 \text{ Gy}^{-1}$ was used.

Profiles in x and y direction were generated for the spot and line patterns. For the spot pattern, the cuts were placed through the centre of the spots, while for the line patterns six equally distributed cuts were made orthogonal to the irradiated pattern. A comparison of the fluence distributions of the static and the compensated case at the same position reveals the lateral motion compensation performance of the system. Due to the shape of the beam profile the cross sections through the particle fluence are of approximately Gaussian shape. A statistical analysis of the relative shift between the peaks in the static and compensated cases quantifies the accuracy of compensation. The film signals of the moving cases were not analysed quantitatively, but they are shown to visualise the influence of target motion during irradiation.

In case of the homogeneous square, two orthogonal line profiles proof the performance of 3D-OMC. In addition, the dose homogeneity was calculated according to eq. (4.1). The influence of the finite dose fall-off was eliminated by reducing the ROI size by ± 5 mm to 110×110 mm² (cf. chapter 7.1).

7.2.3 Results and Discussion

Fig. 7.4 shows the images of the film signal for the spot pattern. The moving films clearly show, that the regular orientation of the spots is heavily distorted in the presence of target motion. The spots are displaced and smeared over the volume. With 3D-OMC enabled, the spot pattern was restored, using a rate of motion compensation (data update rate) of 10 Hz.

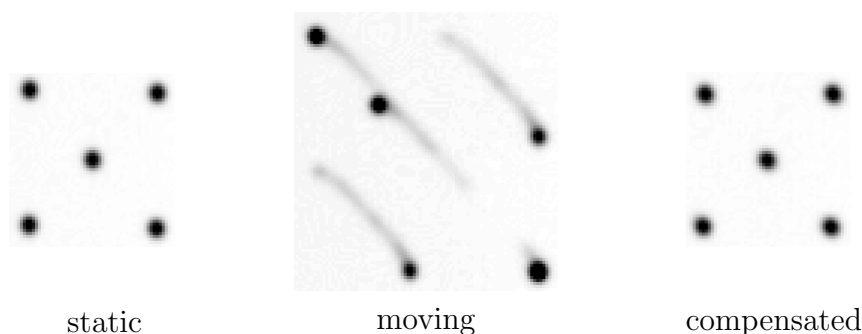


Figure 7.4:

Measured film signal for a stationary target (static) and a target undergoing a 2D, respiration-like motion during the irradiation (moving). In the compensated case, the target was moving with the same pattern as in the moving case, but the automatic motion compensation (3D-OMC) was activated. Brightness and contrast of the images were adjusted to improve visibility.

In fig. 7.5 fluence profiles through the spot centres are shown for the compensated and static case. The profiles (S1-S6) are derived from line cuts through the film signal at the positions indicated in the images. According to the beam profile, the spots have a 2D Gaussian fluence distribution. Width and position of the Gaussian peaks in the fluence profiles were determined in x and y direction for each of the spots. While the width of the peaks remained almost unchanged, some of the peaks in the compensated case were slightly shifted with respect to the static case. A statistical analysis over all five points revealed an average shift of 0.016 ± 0.213 mm in x and -0.013 ± 0.206 mm in y direction. The average shift depends on the positioning accuracy of the films relative to each other. The statistical distribution

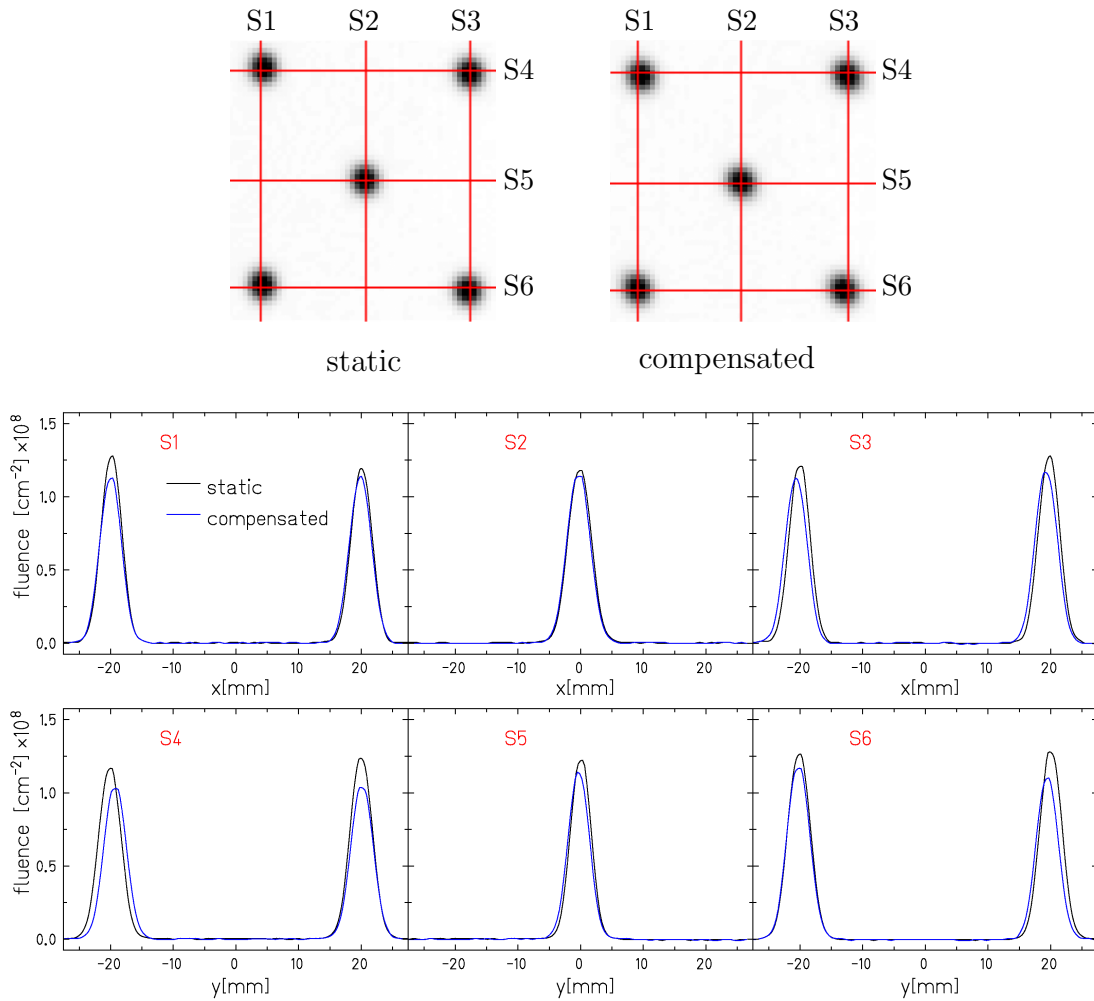


Figure 7.5:

Comparison of the measured film signal of the static and compensated point pattern. The fluence profiles show line cuts through the two-dimensional film signal at the positions marked in the upper images.

of the shifts⁴, on the other hand, is independent of the film position and indicates the motion compensation accuracy. Apparently, the integral of the fluence signal differs for single peaks. This can be explained by a slight rotation of the two films relative to each other. In this case, the line is positioned exactly in the centre of one spot and slightly off centre for the other. Assuming a symmetrical particle fluence this does not have any effect on the peak position in the profiles.

The spot pattern represents a very simple, but not realistic case: The beam is deflected to one position at the beginning of a spill and stays at this position for at least one spill. Comparing the fluence distribution in the static and compensated case reveals the pure precision for online realignment of the beam by the 3D-OMC system. The results show that this precision is better than ± 0.25 mm in each direction.

In reality, the pure motion compensation is superimposed by the general scanner motion in a sequence of points. To probe the compensation accuracy under realistic conditions, two orthogonal line patterns were irradiated.

Fig. 7.6 shows the film signals for the line patterns. In both cases (horizontal and vertical lines), the target moved orthogonal to the line orientation. For the

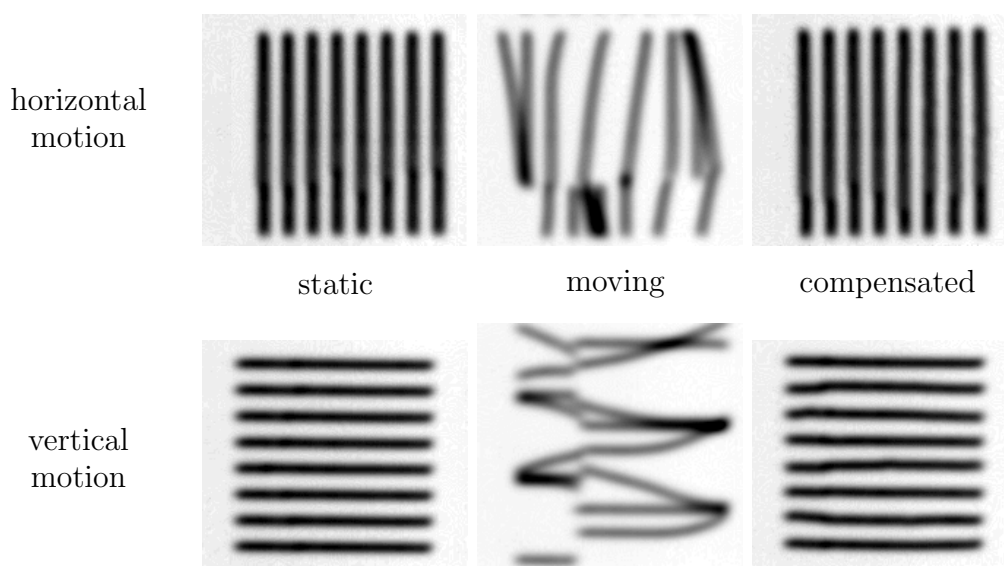


Figure 7.6:

Measured film signal for a stationary target (static) and a target undergoing a 1D, respiration-like motion orthogonal to the scanning motion (moving). In the compensated case, the target was moving with the same pattern as in the moving case, but the automatic motion compensation (3D-OMC) was activated. Brightness and contrast of the images were adjusted to improve visibility.

⁴represented by the standard deviation given as the error on the measured values

compensated measurements, the motion update rate was set to 10 Hz. As expected, the patterns are heavily distorted in the moving cases. The lines are neither straight nor equally spaced. With 3D-OMC activated, the line patterns are restored.

In fig. 7.7 and 7.8 fluence profiles of the static and compensated case are shown for the horizontal and vertical line patterns, respectively. The cross sections through the lines are of Gaussian shape. As for the spot pattern, the shift in peak position between the static and the compensated case was determined. The statistical analysis over all lines and cuts revealed a larger error in the motion compensation than for the spot pattern. The average shift in beam position was 0.364 ± 0.368 mm in

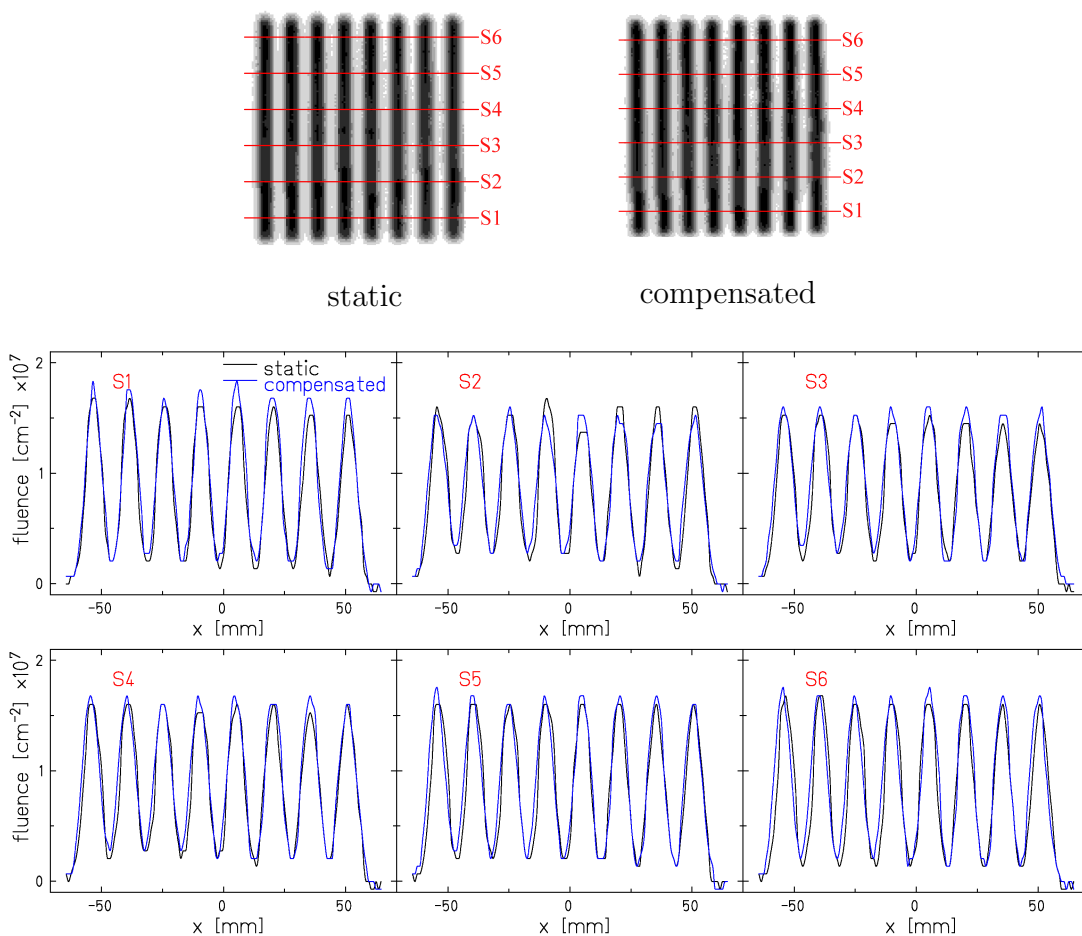


Figure 7.7:

Comparison of the measured film signal of the static and compensated vertical line pattern. The profiles show line cuts through the two-dimensional film signal at positions marked in the upper images. Online motion compensation was performed with motion data update rate of 10 Hz.

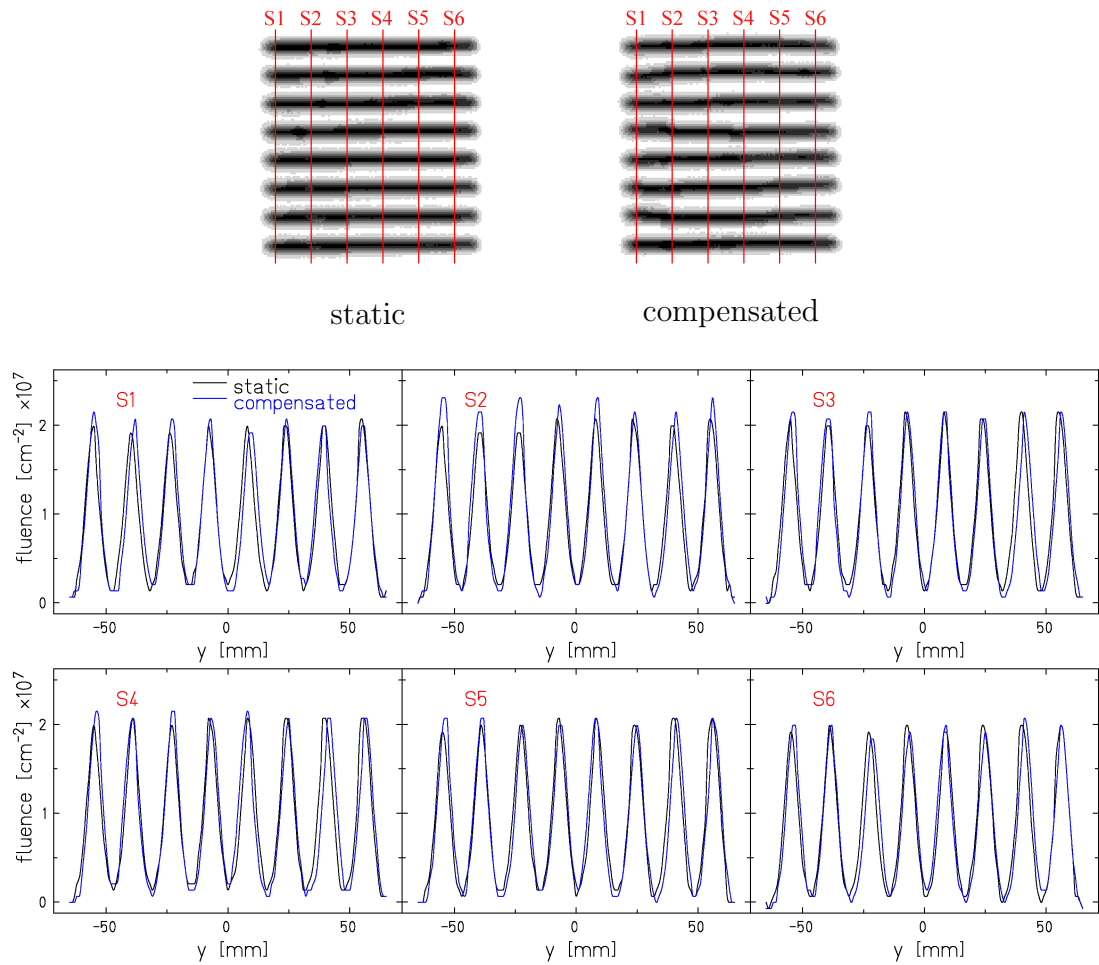


Figure 7.8:

Comparison of the measured film signal of the static and compensated horizontal line pattern. The profiles show line cuts through the two-dimensional film signal at positions marked in the upper images. Online motion compensation was performed with a motion data update rate of 10 Hz.

x and -0.474 ± 0.497 mm in y direction. The additional inaccuracy of 0.2-0.3 mm reflects the pointing accuracy of the raster scanner of approximately 1‰ of the maximum scanning field (± 200 mm) [Hab]. For the spot pattern this effect averaged out due to the longer irradiation times per spot.

The compensation accuracy can further be improved by increasing the compensation rate. A shorter time interval for the update of the motion measurement reduces the distance which the target travels unaccountedly. As an example, fig. 7.9 shows the effect of a ten times higher compensation rate for fast scanning in y direction (horizontal line pattern). Compared to the 10 Hz case, the remaining inaccuracies

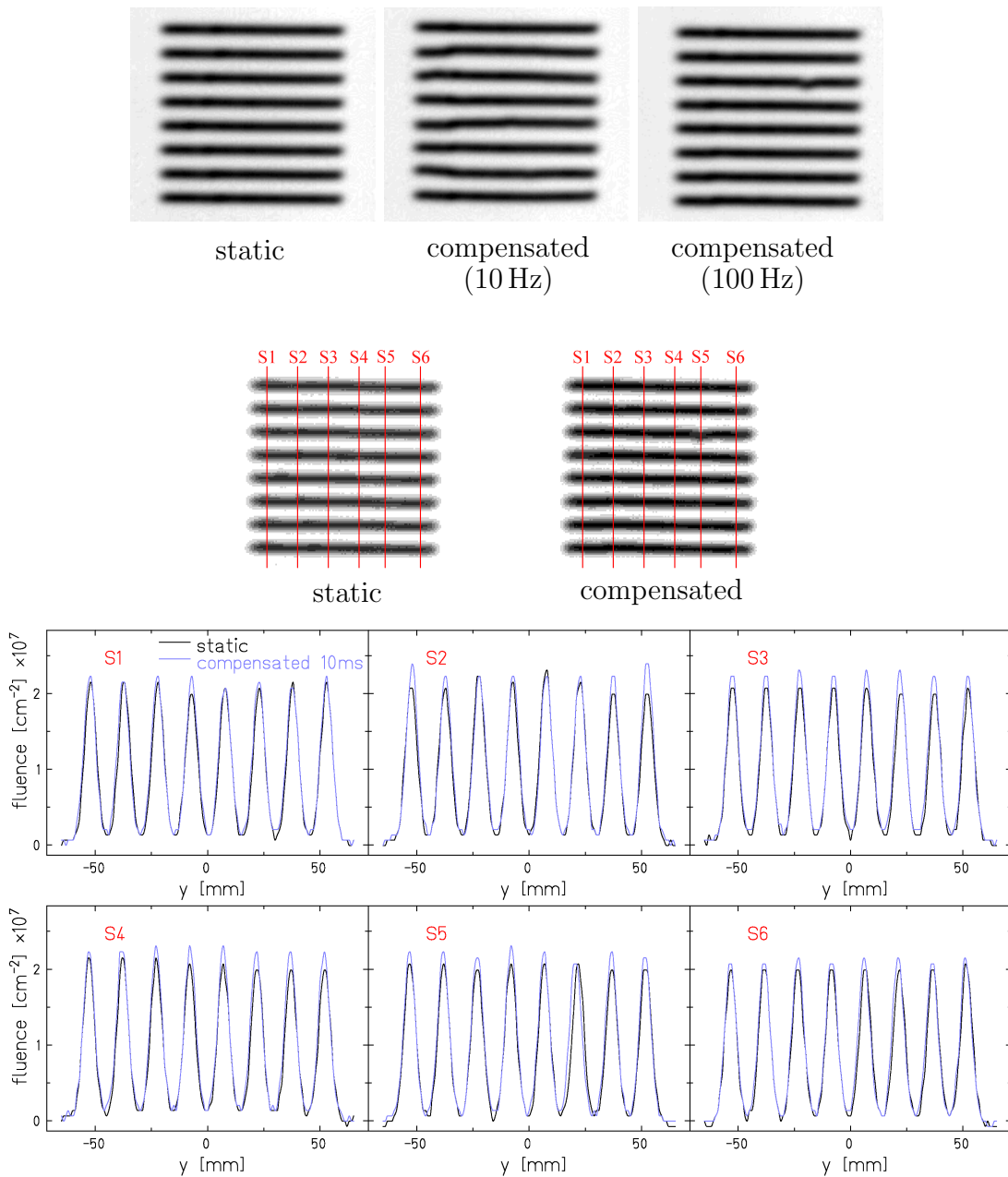


Figure 7.9:

Vertical motion compensation with different target position update rates.

The upper part shows the measured film signal for a static and moving target, the later with 10 and 100 Hz update rate. Brightness and contrast of the images were adjusted to improve visibility.

The lower part shows profiles through the 2D film signal of the static and with 100 Hz compensated case at positions marked in the images in the middle part.

are visibly reduced using a compensation rate of 100 Hz. In the 100 Hz compensated case, the third line from the top exhibits a single, significant deviation from the static case. This is most likely due to a short loss of time correlation between the measured motion signal and the compensation process. Such a loss of data correlation can automatically be detected and accounted for, once the compensation is fully included into the scanning control system. But with the prototype setup bypassing all consistency checks of the dataflow within the SCU, such deviations remain undetected during the experiment. The fluence profiles for the increased compensation rate, shown in the lower part of fig. 7.9, were analysed with respect to the peak positions. With an increase of the compensation rate from 10 Hz to 100 Hz, the average shift was reduced from -0.474 ± 0.497 mm to 0.176 ± 0.221 mm. As the motion related contribution is suppressed by a factor of 10, the remaining inaccuracy is due to the precision of the raster scanning system.

In summary, depending on the update rate, a lateral compensation accuracy of $< \pm 0.25$ mm in both directions can be achieved with the 3D-OMC prototype setup. A realistic irradiation pattern consists of 2D extended regions filled with dose, which are composed of single lines positioned close enough to each other to yield a smooth dose distribution. Any deviation in the compensated position has a direct effect on the dose homogeneity. To investigate the consequences of the compensation accuracy on the dose deposition, a homogeneously filled square pattern was investigated.

Fig. 7.10 shows the measured film signals for the homogeneous square for different motion directions. In the first row, the moving and compensated images are shown for a purely horizontal target motion (x direction), in the second row for a purely vertical motion (y direction) and in the third row for a superposition of x and y motion. The motion parameters were the same in all cases. The measurements were performed with 10 Hz as well as 100 Hz compensation rate. The images for the moving cases are scaled (see axis). The dashed line marks the PTV and the solid line the reduced ROI excluding the region of finite dose fall-off.

Apparently, the influence of the same target motion amplitude is different for the two lateral directions. This is easy to understand, since in this experiment the scanning direction is not switched, when changing the direction of target motion. Consequently, the target motion is parallel to the scanning motion in one case and orthogonal in the other. As the plane is irradiated line-by-line, a parallel target motion (x) smears the dose continuously along the scanned lines. An orthogonal component (y and xy), on the other hand, scrambles consecutive lines. Spaces occur which are not irradiated at all, and those, where the lines cross each other, receive too much dose. In general, a motion component orthogonal to the fast scanning component has the largest effect on the dose distribution (cf. chapter 4.3.2). With enhanced contrast, the differences in the dose homogeneity for 10 Hz and 100 Hz compensation rate are visible. Although the shape of the 2D dose distribution was already restored with 10 Hz, small inhomogeneities remained. The inhomogeneities

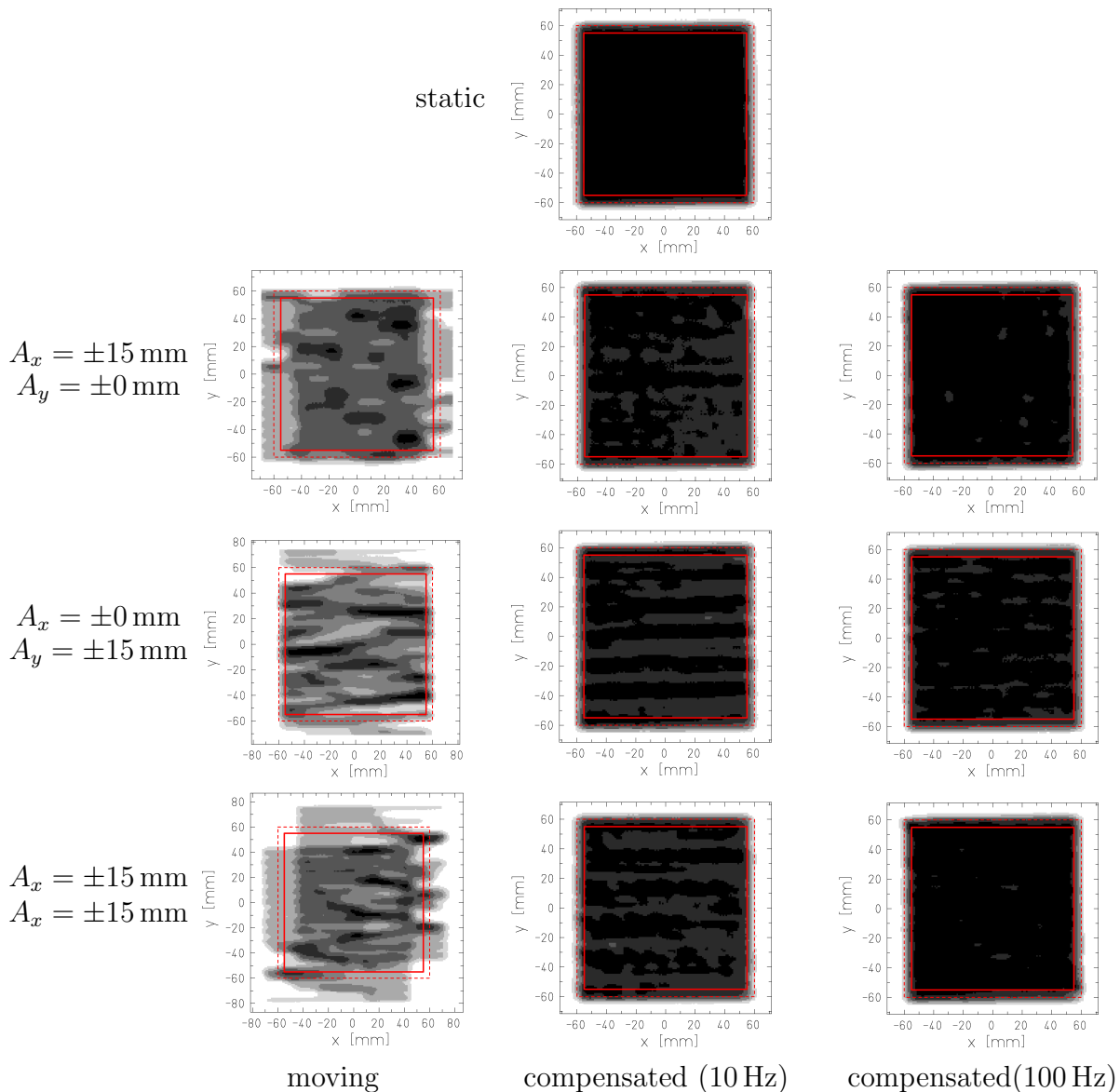


Figure 7.10:

Measured film signal for a homogeneously filled square for different motion directions (first row: purely horizontal, second row: purely vertical, third row: horizontal and vertical superimposed). The solid line marks the reduced target boundary used for the calculation of the dose homogeneity while the dashed line indicates the real target contour used for the determination of the fraction of dose deposited outside. Note: The moving case images are out-of-scale! Brightness and contrast were adjusted to improve visibility.

in the dose distribution diminished when using 100 Hz compensation rate. Fig. 7.11 shows this effect in more detail by means of dose profiles through the centre of the plane. For a motion purely parallel to the fast scanning direction (x direction) the dose profiles of the static and compensated cases agree very well for both compensation rates. If the target moves orthogonal to the fast scanning direction (motion in y direction) the dose profiles measured 10 Hz motion compensation show position dependent differences in the deposited dose of more than $\pm 10\%$ compared to the static case. An increased rate of 100 Hz leads to a smooth dose distribution which matches the static distribution very well.

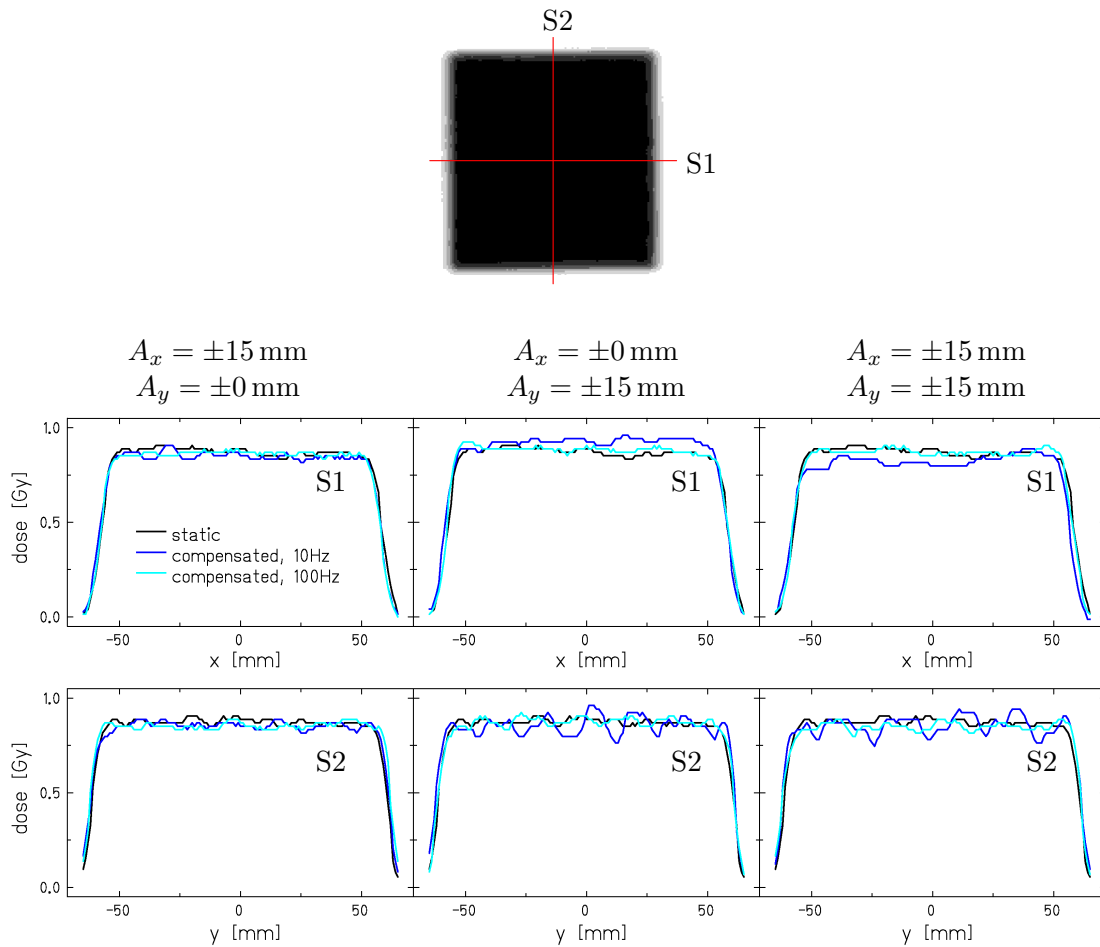


Figure 7.11:

Dose profiles through the centre of the square pattern, as marked in the upper sample image, for different motion conditions and compensation rates. The dose distribution for a compensation rate of 10 Hz agrees very well with the static case but was improved using a higher compensation rate of 100 Hz.

| | moving | compensated (10 Hz) | compensated (100 Hz) |
|-------------------------------|--------|------------------------|-------------------------|
| $\vec{A} = \pm(15, 0, 0)$ mm | 0.763 | 0.959 | 0.961 |
| $\vec{A} = \pm(0, 15, 0)$ mm | 0.668 | 0.931 | 0.965 |
| $\vec{A} = \pm(15, 15, 0)$ mm | 0.665 | 0.931 | 0.963 |
| static | | 0.969 | |

Table 7.3:

Dose homogeneity inside a homogeneously painted square (size: 120x120 mm²) for different motion amplitudes \vec{A} . To exclude the effect of the dose fall-off, only the inner 110x110 mm² (solid lines in fig. 7.10) are taken into account.

Tab. 7.3 shows the calculated dose homogeneity over the reduced ROI, marked in fig. 7.10, for all plane measurements. As expected, the homogeneity is drastically reduced by an uncompensated target motion. Target motion parallel to the fast scanning direction results in a homogeneity of $\approx 76\%$ compared to 96.9% in the static case. Orthogonal target motion even further diminishes the homogeneity to $\approx 67\%$. To evaluate the significance of these values one can refer to the limits specified in the approval of operation of the GSI facility for medical application. According to this document, the mean variation to the planned dose distribution has to be less than $\pm 5\%$ in order to be allowed to apply the treatment to a patient. If the variation is larger than this value but lower than 20%, the application is allowed under certain conditions, if medical reasons exist. Plans with a dose deviation larger than 20% are not allowed for patient application under any circumstances [Hes97]. It has to be emphasised, that the approval of operation does not include moving targets, but the specified values indicate the limits considered to allow a safe patient treatment under medical, technical and legal aspects. Comparing the measured dose homogeneity to the limits of the approval of operation, the uncompensated application to a moving target would not be possible at all. 3D-OMC would raise the homogeneity far enough to correspond to restricted and, with 100 Hz update rate, even to general applicability⁵.

7.3 Longitudinal Online Motion Compensation

The most critical issue of online motion compensation in ion irradiation is the inclusion of the longitudinal motion component. The position of the Bragg peak

⁵Note: None of the described components has any kind of approval for medical application. Therefore, the comparison is purely hypothetical and does not imply any real applicability on patients, yet. But being already accepted for the static case the quoted limits provide an objective for the design and the feasibility of the motion compensation system.

is influenced by changes in the WEL in front of the target. Due to the sharp dose fall-off at the distal end of the heavy ion Bragg peak, the deposited dose can differ by up to 100 % from the expected value, if the density variations are large enough to shift the peak position behind the planned dose tail region. Therefore, the longitudinal motion component cannot be neglected when performing online motion compensation with ion beams (cf. chapter 3.4.3).

In the following section, the longitudinal compensation performance of the prototype setup for 3D-OMC is investigated.

7.3.1 Experimental Setup

For the feasibility study a change in WEL in front of the target volume was simulated with two different methods: First, the general functionality was tested by requesting different energies from the accelerator which lead to a shift of the Bragg peak position during the irradiation of a single IES. The energies were changed from spill to spill and the actual setting was extracted in real-time from the status information of the accelerator by a dedicated CAMAC module. Secondly, a compressible rubber ball, filled with water, was irradiated with a fixed energy. During the irradiation, the ball was compressed and expanded periodically by a piston. The position of the piston and thereby the state of deformation was indirectly determined by the rotation angle of the driving motor. The calibration curve between motor position and ball extension parallel to the beam was determined in advance (cf. chapter 6.2.3). The maximum change in WEL was measured to be 12.16 ± 1.56 mm.

In both cases, the longitudinal compensation accuracy was verified by the depth dose distribution measured with the water column setup. During the tests with varying energy the water column setup was placed in the isocentre. In the experiment with the deforming ball the water column was placed directly behind the ball, which was placed in the isocentre.

Four different experiments were performed in the feasibility study for longitudinal motion compensation:

1. To verify the effect of the wedge material on the depth dose distribution, the Bragg peak was measured twice for the same energy, once without the wedges and once with the static wedges at their reference position in the beam.
2. To test the compensation accuracy, three different energies were alternately requested and 3D-OMC was used to correct for the position of the middle energy. The minimum and maximum energies differed by approximately $32 \frac{\text{MeV}}{\text{u}}$, corresponding to a change in depth of 27 mm.

3. To verify the high dynamics of the wedge drive, six equally distributed energies over the same energy range as before were requested in a random order. One of the six energies was taken as reference for the motion compensation.
4. With the water filled rubber ball a continuous change in WEL was achieved. 3D-OMC was enabled to correct for the state of maximum expansion. A typical period for respiration-related motion would span over a few data points only, averaging out the effect on the dose distribution. The effect was enhanced by increasing the time period of deformation to 57 ± 2 s corresponding to the time required for scanning the region around the Bragg peak.

7.3.2 Data Analysis

The analysis of the peak position is impeded by variations of the detailed form of the Bragg peak. To determine the relative shift, two curves were overlaid in one graph at the same position. The relative shift was taken as the offset required to match one curve to the other over a large range (entrance channel and dose tail). This way, the shift can be determined with a higher precision than the step size of the water column measurement.

7.3.3 Results and Discussion

In a first step, the effect of the wedge material on the depth dose distribution was studied. For this purpose, the depth dose distribution was measured twice, with and without the wedges at the reference position in the beam. Fig. 7.12 shows the results of this experiment. To compare both curves, the data set including the wedges is shifted in depth by 56.4 mm, which corresponds to the thickness of the wedges at the reference position. The small difference to the calculated wedge thickness (cf. appendix D) is the result of inaccuracies in setting the reference position. In the prototype setup, the wedge drive is equipped with incremental linear encoders, requiring a reference run at the beginning of each experiment. This reference run is based on mechanical proximity switches and has an intrinsic accuracy of $\approx \pm 0.45$ mm in the resulting WEL (± 0.25 mm in wedge position). To extract the reference thickness with a higher precision, the actual reference conditions were verified experimentally at the beginning of each measurement involving the wedge drive. All data presented below are corrected on the actual, measured reference conditions. This inaccuracy can be eliminated by using absolute linear encoders. Compensated for the wedge thickness, both curves match perfectly, showing the negligible influence of the PMMA on the depth dose distribution.

The longitudinal compensation performance of the 3D-OMC setup was tested using three different energies, which differed by 27 mm in range. The energies were requested alternately, spill by spill, and automatically compensated by the 3D-OMC

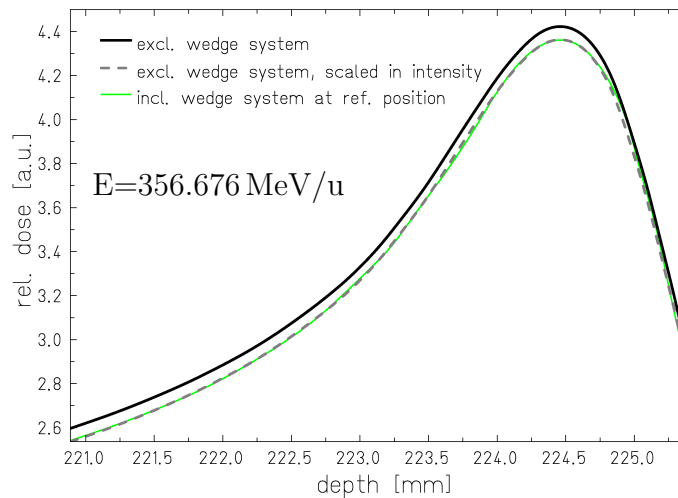
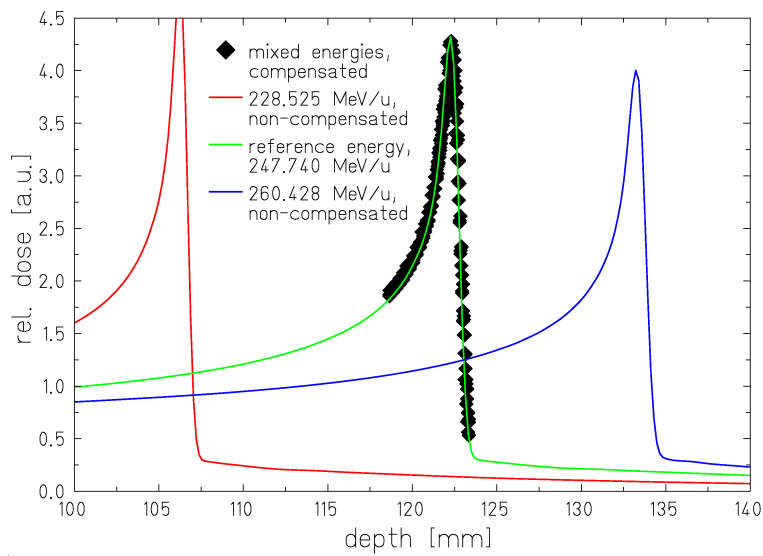


Figure 7.12:

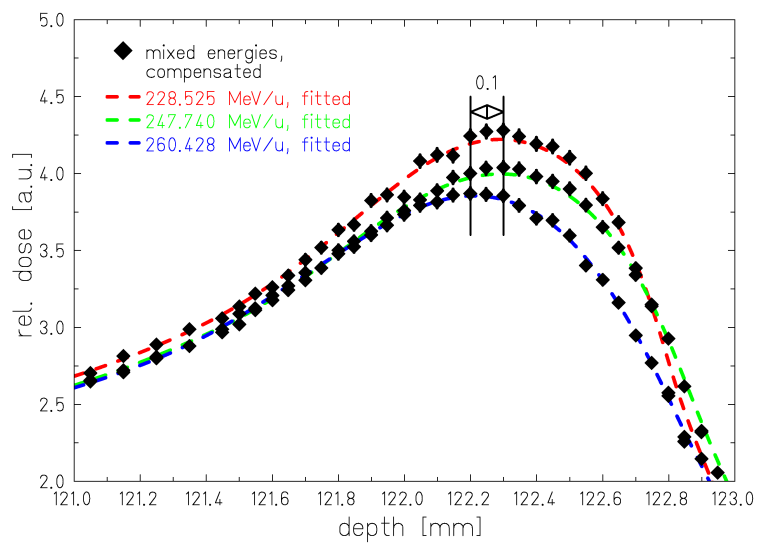
Influence of the plexiglass wedges on the beam profile. The measured depth dose distributions with and without wedge drive are compared. The data with the wedges is corrected for the WEL of the drive at the reference position. (Most of the error bars on the data points are smaller than the symbols.)

system to match the middle energy. Fig. 7.13 shows the results of this experiment in a wide-range view (a), including the measured peaks for the uncompensated irradiation, and a close-up (b) on the compensated curve. The compensated curve consists of three data points per depth interval, one for each energy step. A separate curve was fitted to each of these three subsets to extract the compensated position. The peak positions of the resulting curves agree well within the accuracy of the water column measurement (0.10 ± 0.05) mm, which is $< 1\%$ of the total compensated distance. The difference in height between the three distributions is due to the increased WEL in front of the peak. If the plateau region spans over a longer distance the fraction of integral dose deposition in the peak is decreased compared to the plateau region. This behaviour is not unique for the longitudinal compensation strategy and is already included in the treatment planning for static target volumes. When dealing with realistic target motion, 3D-OMC will directly compensate a change in the WEL (e.g. substitute bone by PMMA) at constant initial energy and the integral WEL will be the same. Therefore, no reduction in dose deposition is expected and the depth dose distribution will remain unmodified as shown in fig. 7.12.

The alternate processing of energies fixes a pattern of motion for the wedge drive. To verify the performance with arbitrary changes, the same energy range was divided into six intervals, which were switched from spill to spill in a random order. 3D-OMC was set to automatically compensate for a reference energy. Fig. 7.14 shows



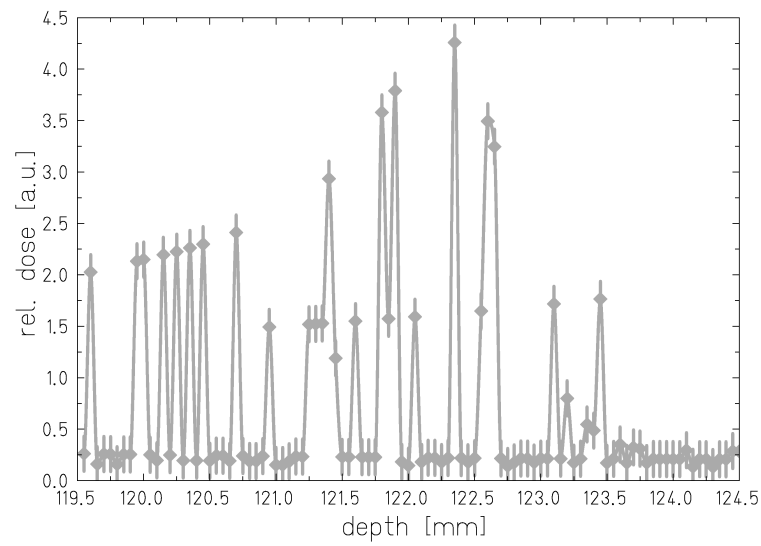
(a) wide-range



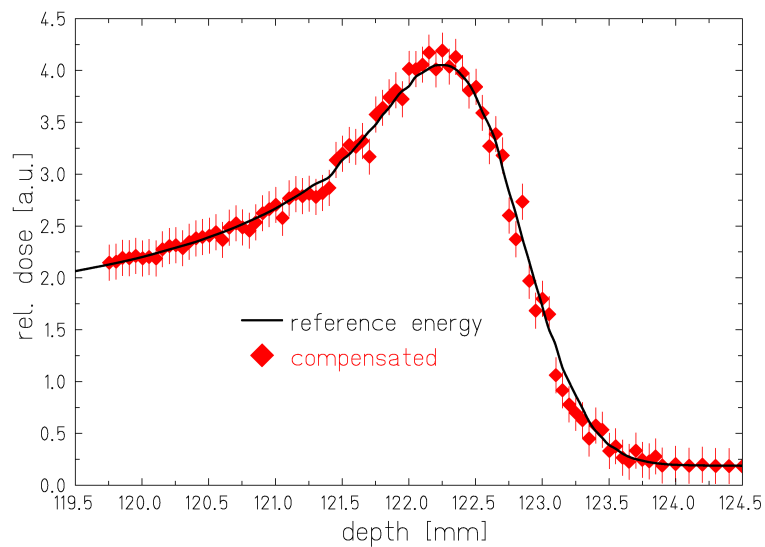
(b) close-up

Figure 7.13:

Three energies alternately requested spill by spill and automatically compensated to match the middle energy (a). For each depth interval three consecutive spills were measured, yielding a data subset for each energy (b). The horizontal error bars on the data points are smaller than the symbols.



(a) non-compensated



(b) compensated

Figure 7.14:

Dose distribution for a random energy variation with 3D-OMC dis- (a) and enabled (b). The black curve represents the reference energy for the automatic motion compensation. The horizontal error bars on the data points are smaller than the symbols.

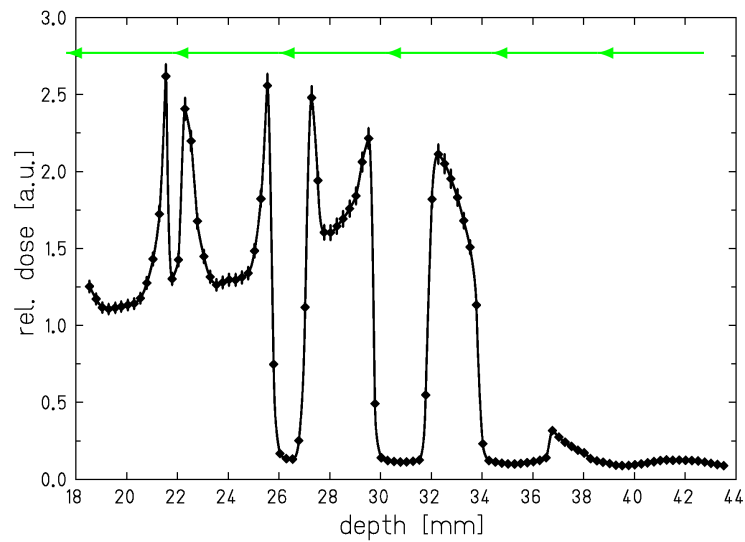
the completely destroyed depth dose distribution in the uncompensated case (a), as well as the restored distribution with 3D-OMC activated (b). The error bars in y direction account for the WEL related variations in relative dose deposition discussed above. The few deviations from the expected curve correspond to a displacement by one depth interval (0.05 mm) of the water column measurement, which is in good agreement with a compensation accuracy of $< 1\%$ as determined above. As expected, the longitudinal compensation of 3D-OMC works very well for random displacement values. But still, the changes in the displacement occurred in discrete steps after a fixed time interval (every 5 s).

To test the 3D-OMC system under realistic conditions of a continuous longitudinal displacement, the depth dose distribution behind a deforming, water filled ball was measured. Fig. 7.15 shows the measured depth dose distributions for the non-compensated (a) and the compensated case (b). The non-compensated curve clearly shows the deformation pattern. Over the range of the measurements, five full motion cycles (indicated by green arrows) can be seen, a sixth occurred in the dose tail region, which is due to its flat gradient insensitive to target motion. With 3D-OMC enabled the dose distribution is largely restored. Only two groups of data points show significant deviations from the reference curve. These groups are separated by almost a full motion period and the deviations agree with the uncertainty in the displacement information (cf. chapter 6.2.3). These two findings strongly imply that the deviations are related to an inaccurate determination of the deformation state. In general, the dose distribution was well restored by the 3D-OMC prototype setup. A systematical error in the compensation or a more frequent failure of the drive would have a large effect in the proximal plateau region, which spans over two motion periods. Further proofs of the reliability of the longitudinal motion compensation require a more sophisticated motion phantom and independent, e. g. optical, motion tracking.

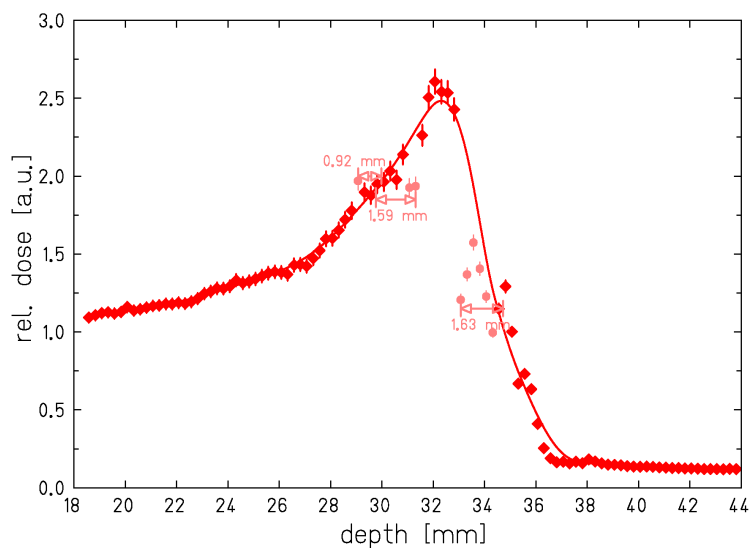
7.4 Lateral Online Motion Compensation on Complex 3D Target Volumes

The effect of online compensation of respiration-like, lateral motion was tested on complex, in 3D extended target volumes⁶. To fill an extended target volume homogeneously with dose, the number of ions has to be optimised for each voxel. In general, extended target volumes require an inhomogeneous ion fluence over the target volume. In addition, different iso energy slices are precisely stacked in depth. As a result of such an inhomogeneous irradiation, complex target volumes are highly sensitive to deviations in target motion.

⁶Limited by the use of the 3D positioning table (cf. chapter 6.1), longitudinal target motion could not included in the current study.



(a) non-compensated



(b) compensated

Figure 7.15:

Depth dose distribution measured behind a periodically deformed, water filled ball. In the non-compensated case (a), the depth dose distribution is heavily distorted. The green arrows indicate the six motion cycles (length but not phase) during the measurement. The distortions are eliminated when 3D-OMC is activated (b). The remaining deviations (light red) are due to inaccurate displacement information. Most of the horizontal error bars on the data points are smaller than the symbols.

7.4.1 Experimental Setup

Target motion was induced by means of the 3D positioning table, moving periodically in the two lateral directions. To measure the 3D dose distributions two different detectors were used: a stack of x-ray films and polymeric BANGTM gels. For each pattern, three conditions were compared: the irradiation of a static and a moving detector, the latter with (compensated) and without (moving) 3D-OMC enabled. The motion information was taken from encoders attached to the axes of the positioning table. The data update rate for motion compensation was set to 100 Hz.

The motion amplitude in x and y direction was set to ± 15 mm. Due to technical reasons, the frequency of the motion was with 9-12 s slower than a typical respiration-related target motion. To yield a smooth motion pattern, the table was operated in accelerated mode.

To test the compensation performance on an extended target, two different target geometries were studied, a spherical target volume and a volume corresponding to the tumour of a patient which has been treated at GSI under stereotactic fixation. The spherical target volume measured 30 mm in radius and was centred in a WE depth of 50 mm. To irradiate this volume, 29 different energies ranging from 102 to 195 MeV/u were required. The irradiation took about 3.5 min. The resulting dose distribution was measured with the film stack equipped with films sandwiched between polyethylene (PE) spacers of 10 mm thickness. The film box was aligned to the isocentre of the beam. A dedicated reference frame for inter-film alignment and a calibration wedge for determination of the saturation optical density were irradiated on the films.

A more complex target geometry was given by one field of the optimised, static treatment plan of a former patient⁷. The optimised, physical dose distribution is shown superimposed on the planning CT image in fig. 7.16. In the upper figure (frontal view) the sharp lateral and distal dose fall-off, achieved for a static tumour, can be seen. Due to the small lateral scattering and the sharp, distal dose fall-off of the carbon beam coming from the right, the dose drops within a few mm from therapeutic level (red, 95-105% of the prescribed dose) to the lowest dose interval (dark blue, less than 20% of the prescribed dose). The lower figure (sagittal view) shows the orthogonal direction in beam's-eye-view. The brain-stem as OAR is perfectly spared with the optimised treatment parameters. Although a tumour at the same location will never show any target motion, this optimised patient plan was taken as an example for the irradiation of a complex, moving target volume. For each of the three motion conditions (static, moving, compensated) the unmodified treatment dataset was irradiated on a separate polymeric BANGTM gel. For the irradiation, 44 different energies ranging from 135 to 278 MeV/u (corresponding

⁷This patient was treated at GSI using stereotactic fixation and the tumour was not subject to any target motion. The plan was only taken as an example for a complex target volume.

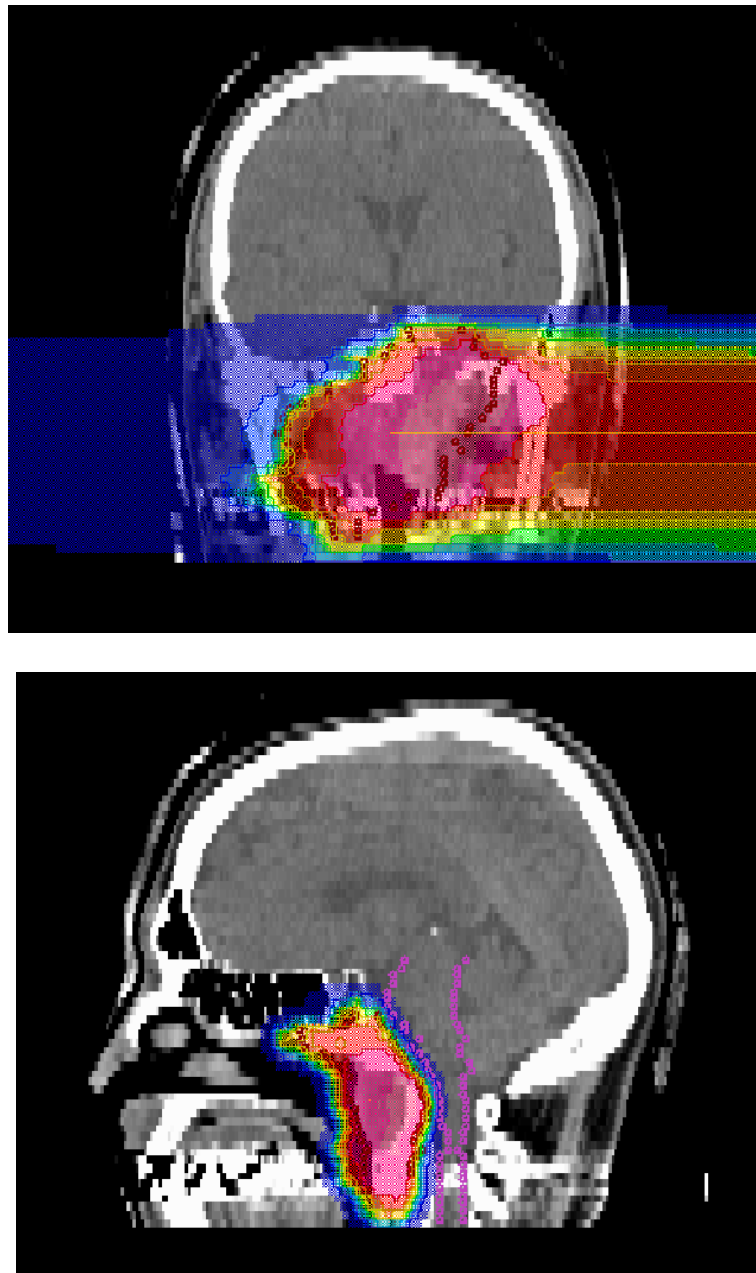


Figure 7.16:

Planned, physical dose distribution of a patient treatment overlaid on slice images of the planning CT. The top figure shows the frontal view with the beam coming from the right. The bottom figure shows the orthogonal, sagittal view.

to approximately 4-15 mm WEL) were required. The total irradiation took about 4.2 min. Reference marks and a calibration wedge were added with the BANGTM gels resting in the isocentre.

The magnetic resonance imaging (MRI) analysis of the gels was performed with a 1.5 T whole body scanner⁸ at the DKFZ⁹ in Heidelberg. The MRI sequence was based on the turbo-spin-echo technique [Hen86] with a turbo factor of five, extended with the echo-sharing technique [Lis92]. The repetition and echo times were set to $T_R = 12000$ ms and $T_E = 30, 60, 90, \dots, 420$ ms, respectively. The field of view measured 256 mm and a matrix size of 256×256 was chosen, yielding a lateral resolution of 1×1 mm². The volume was scanned in slices of 4 mm thickness.

7.4.2 Data Analysis

The single films of the extended target volume were analysed in the same way as described above for the 2D film dosimetry. A background of 0.23 was subtracted and the net optical density was normalised to $optD_{max} = 4.02$. The dose distribution was shifted in lateral direction to the isocentre using the reference frame irradiated on all of the films. The longitudinal film position was corrected by the WEL of all proximal material. The measured optical density distribution was compared to the calculated (simulated) film signal according to the planned radiation field in the treatment planning software. In contrast to the experiments with 2D targets in chapter 7.1 and 7.2, the optical density was not directly converted to dose, since the composition of the radiation field was not precisely known for the 3D irradiation. The quantitative analysis included the comparison of the film homogeneity over all films of the sphere. The influence of the dose fall-off on the homogeneity was minimised by considering a reduced VOI. In the current case, a radius of 24 mm was empirically determined as the upper limit for the VOI size, yielding a constant dose homogeneity in the static case. For a position resolved comparison between the static and compensated dose distribution, line cuts were taken in x and y direction through the centre of the ROI in one sample slice.

In contrast to 3D film dosimetry, no quantitative analysis was possible for the BANGTM gel measurements, since the detailed dependence of the measured relaxation rate on the composition of the radiation field is not precisely known, yet. Up to now, the calculation of BANGTM gel signal is not included in the treatment planning software TRiP98. Nonetheless, they provide an excellent spatial resolution in 3D, which is only limited by the MRI measurement. The measured BANGTM gel signals of the three motion conditions were compared qualitatively calculating the position resolved differences in transverse relaxation rate R_2 . The spin-echo MRI technique produces a series of R_2 weighted images. The transverse magnetisation

⁸Siemens Magnetom Vision, Erlangen, Germany

⁹Deutsches Krebsforschungszentrum (German Cancer Research Centre)

signal (S_t) at echo time T_i^E depends exponentially on the transverse relaxation rate R_2 [US03]

$$S_t(T_i^E) = S_t(0) \cdot \exp(-T_i^E/T_2(D)) = S_t(0) \cdot \exp(-R_2(D) \cdot T_i^E) \quad (7.1)$$

with $S_t(0)$ as the transverse magnetisation at an echo time of 0. The distribution of transverse relaxation rate $R_2(D)$ was derived pixel-by-pixel via a linear fit to the logarithm of the time-resolved, T_2 weighted MR signal.

7.4.3 Results and Discussion

An overview on the optical density distribution for the spherical target volume is given in fig. 7.17. The 2D film signal distribution of the three motion states is compared at three different depths: in the entrance channel (3.0 mm WE depth, top row), the centre of the target volume (55.8 mm WE depth, middle row) and the distal end cap of the sphere (76.9 mm WE depth, bottom row). In each of the moving cases, the dose is heavily distorted by target motion. The circular ROI in the distal part of the target volume is deformed as a result of the shift in target position between the irradiation of consecutive voxels. As the proximal slices receive some pre-irradiation, the pattern on these films is a superposition of displaced, partially deformed circles of different size. With 3D-OMC enabled, the optical density distribution is largely restored. Fig. 7.18 shows as an example the optical density distribution along a line in x and y direction, respectively, through the centre of the middle slice (55.8 mm depth). Both distributions match with relative deviations smaller than 5.5 %. Since the optical density cannot be directly converted into dose for an extended target, the measured and calculated film homogeneities over the target volume are compared in fig. 7.19 for all cases. As shown in chapter 4.3.1, the lack of precise knowledge of the beam intensity profile due to experimental restriction introduces an uncertainty in the calculation of the dose distribution for a moving target volume. The results show that the general trend of the homogeneity is well described by the simulations, but the absolute values differ by up to 6 %. This value is in good agreement with the estimated influence of the beam intensity profile (cf. chapter 4.3.1). The calculated homogeneities for the static and compensated case are independent of the detailed beam intensity profile. For the static case all treatment conditions are precisely known and in the compensated case an equal target displacement is assumed for the target shift and the following realignment of the beam. Obviously, the homogeneity inside the considered ROI is significantly reduced if the target is subject to unaccounted target motion. The slope of the data points reflects the positive effect of averaging over many displaced slices in the proximal part of the volume. Online motion compensation restores the homogeneity to the same level as for a static target. The average difference in the measured dose homogeneity is $0.2 \pm 0.4\%$.

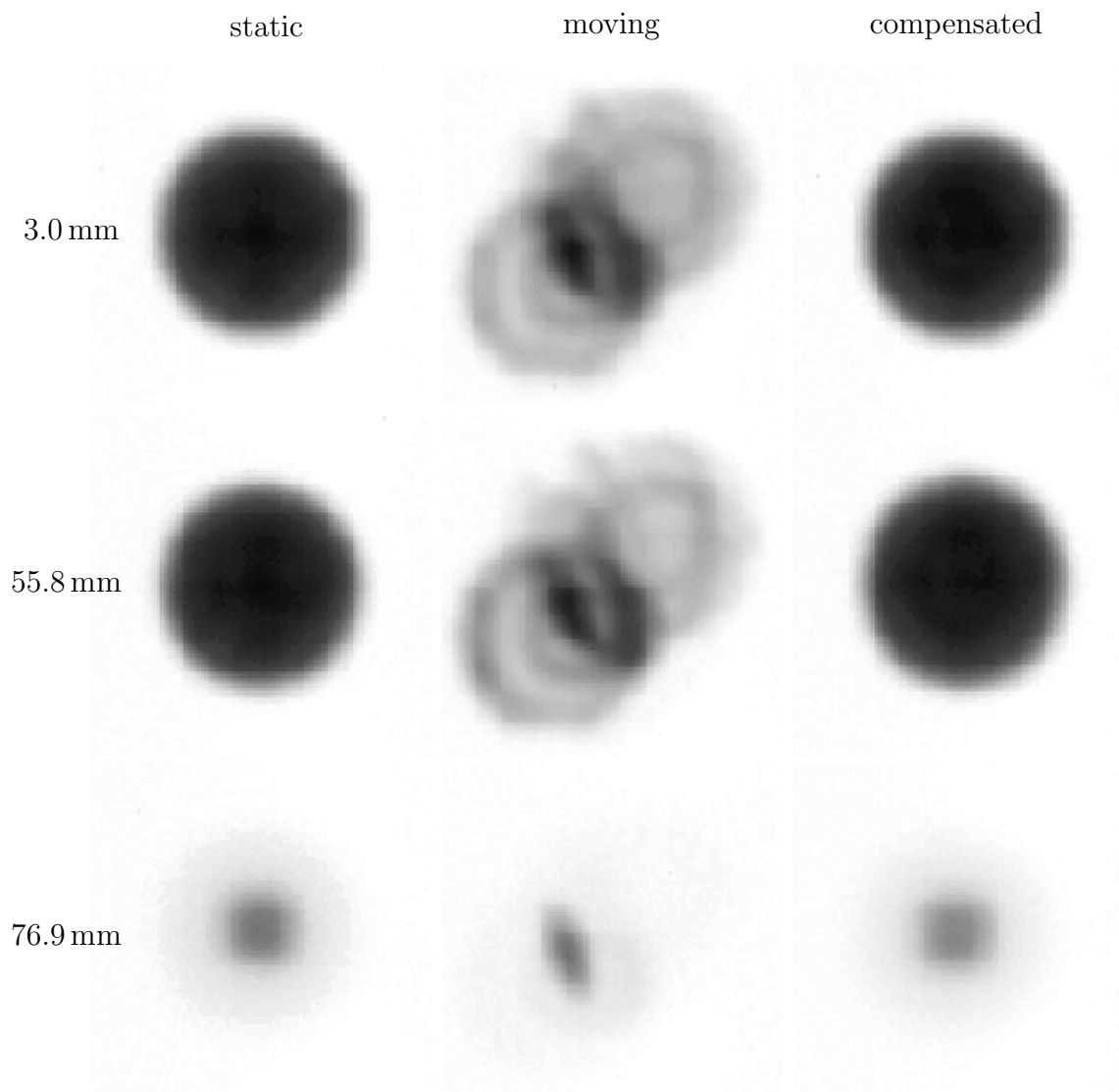


Figure 7.17:

Motion compensation on an extended target volume. Shown are example slices from the entrance channel (3 mm depth, upper row), the middle part of the sphere (55.8 mm depth, middle row) and the distal end of the target volume (76.9 mm depth, bottom row) in static, moving and 100 Hz compensated case, respectively. The target volume consisted of a spherical target volume (30 mm radius, centred in 50 mm WE depth). Brightness and contrast were manually adapted to improve visibility.

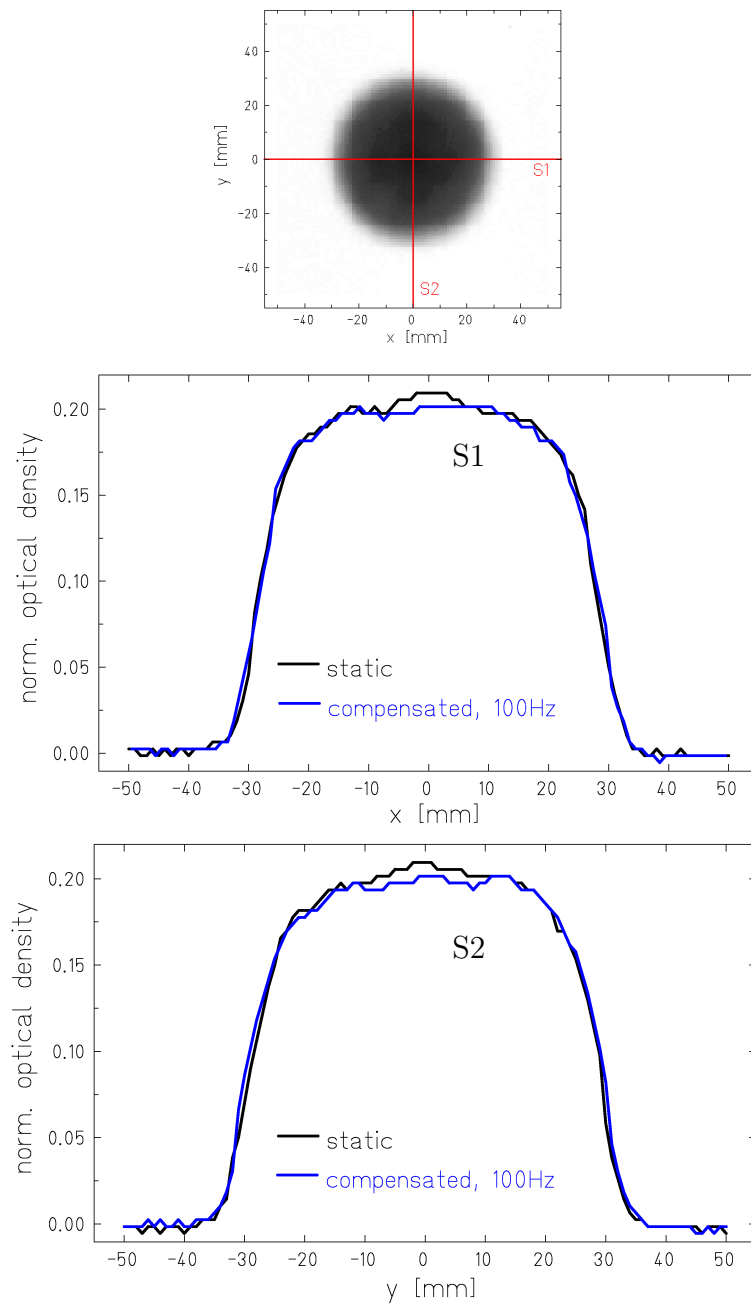


Figure 7.18:

Film signal profiles through the centre of a middle slice (55.8 mm depth) of the spherical target volume from fig. 7.17, as marked in the upper sample image. The measured optical density is shown for a static and a moving target with 3D-OMC enabled (compensated).

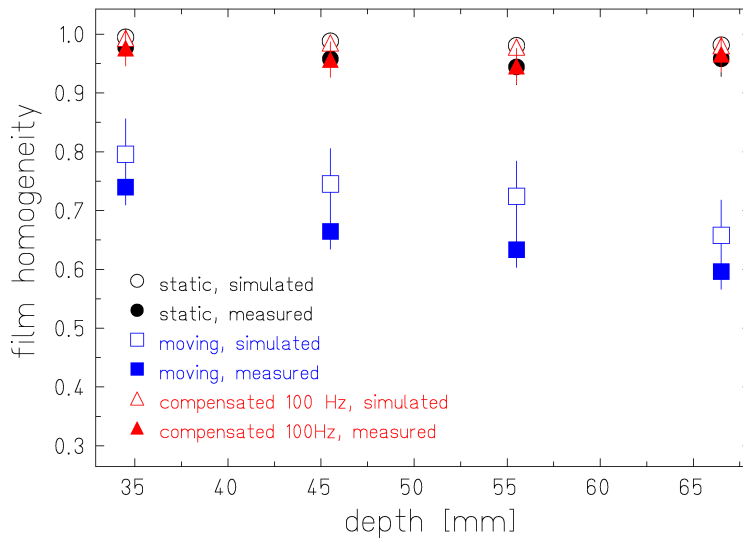


Figure 7.19:

Film homogeneity of a VOI of 24 mm radius, centred in a spherical target volume of 30 mm radius. The measured data is compared to calculations with an extension of the treatment planning environment TRiP98.

To test online motion compensation in a more complex situation, a real patient plan (cf. fig. 7.16) was delivered to a moving BANGTM gel detector measuring the applied dose distribution. Fig. 7.20 shows the dose dependent proton relaxation rate R_2 of the BANGTM gels measured with MRI. The treatment plan was delivered to a static and a moving target volume, the latter with and without 3D-OMC enabled. The image for the moving case visualises the three-dimensional loss of volume conformity in the presence of unaccounted target motion. The low dose region (blue) is significantly enlarged and not regular anymore. The sharp, lateral dose fall-off is heavily distorted. Parts of the low dose region are even melted with the reference wedge, which is clearly separated in the static case. Moreover, in large parts inside the volume the therapeutic dose (yellow) is significantly reduced. With 3D-OMC enabled, the volume conformity is restored. The dose fall-off is sharp and regular again, and the reference wedge is clearly separated. The therapeutic dose region has approximately the same shape and size as in the static case.

The surfaces in the 3D plots mark regions of constant R_2 , but not of the same dose. For monoenergetic beams, the relaxation rate is over a certain dose range directly proportional to the dose [Ram00]. In a mixed radiation field, the strongly non-linear dependence on energy and fragment spectra prevent a conversion into absolute dose with the current knowledge. Until an extensive database is available, only the relative change of the relaxation time can be studied. Fig. 7.21 shows an example of the difference image between the three cases. The data refers to a

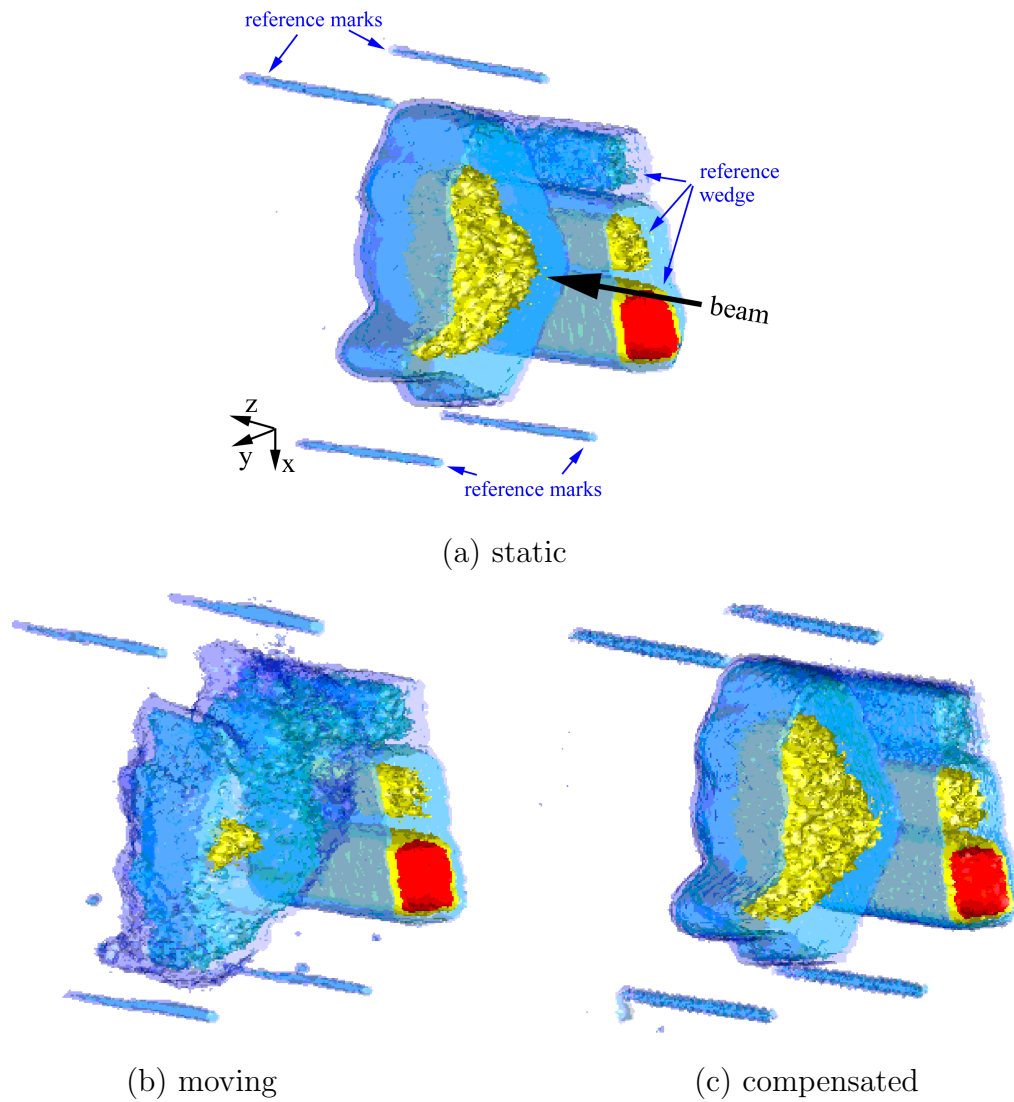


Figure 7.20:

3D distribution of BANGTM gel signal for a realistic patient plan. The images show the distribution of dose dependent proton relaxation times R_2 in BANGTM gels after irradiation, measured with MRI. The gels were irradiated from the right-hand side under three condition: static, moving and with 3D-OMC compensated. A set of four point marks for position alignment encircle the target volume and a calibration wedge consisting of three fields of different intensity (blue, yellow, red) were irradiated on the resting gels.

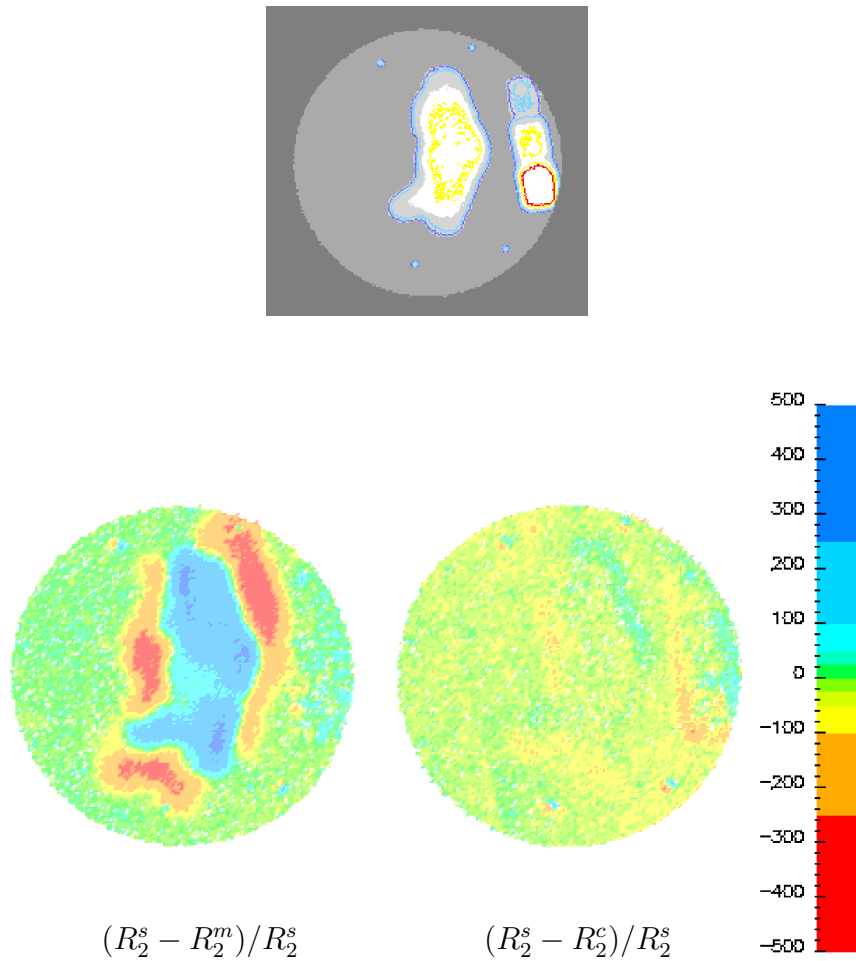


Figure 7.21:

Difference image of the BANG™ gel signals. The static, 2D signal distribution is shown in the upper figure. The bottom left figure shows the relative difference image between the moving (R_2^m) and the static (R_2^s) distribution and the bottom right between compensated (R_2^c) and static. The difference at each voxel is normalised to the corresponding voxel signal in the static distribution. The scale for the different colour levels of the difference images is given in units of [%]. A conversion into dose levels was not possible (see text).

slice in the middle of the target volume (slice no. 24 in 96 mm depth). The static signal distribution in this slice is shown in the top figure. The bottom left figure shows the difference image between moving and static case and the bottom right between compensated and static. The differences are colour-coded according to the right-hand scale in units of [%]. The moving distribution differs significantly

from the static one. In parts of the slice, the deviations exceed $\pm 25\%$ of the voxel signal in the static case. The geometry of the target volume is clearly visible, indicating that the dose to all parts of the target is significantly changed. 3D-OMC eliminates the large differences. In most parts of the slice, the deviations are smaller than 10% , differing not significantly from the background signal in the non-irradiated region. A statistical analysis of the difference in relaxation time between static and compensated case reveals an average deviation of $0.7 \pm 2.1\%$ over the whole slice. It has to be emphasised, that the corresponding difference in dose is not necessarily proportional to the difference in relaxation time. The target geometry is not visible in the difference image between compensated and static case, leading to the conclusion, that 3D-OMC worked as expected, eliminating the motion-related distortions of the dose distribution.

Chapter 8

Summary and Outlook

The aim of this thesis was the investigation of suitable methods for the irradiation of moving target volumes with the magnetic raster scanning system at GSI.

Magnetic raster scanning achieves an excellent volume conformity between applied dose distribution and target volume as long as the target position relative to the reference point of the beam delivery system remains unchanged. Steep lateral and distal dose gradients enable the deposition of a high therapeutic dose in the direct vicinity of organs at risk.

Intensity modulated charged particle therapy is much more sensitive to target motion than other methods of precision radiotherapy (e. g. IMRT), which in principle suffer from the same problems. In practice, the position of the target volume is stabilised by means of stereotactic fixation of rigid, bony structures. This approach fails in the presence of internal motion (e. g. respiratory motion). Interferences between scanning and target motion destroy the volume conformity and wash out the sharp dose gradients. Resulting hot- and cold spots inside the target volume jeopardise tumour control.

Studies from other fields of radiation therapy revealed three basic strategies to irradiate moving target volumes: a controlled interruption of the irradiation as soon as the target volume leaves a pre-defined position window (gating), averaging the dose distribution over several statistically uncorrelated irradiations with reduced dose (rescanning) and an active beam realignment in real-time according to the target displacement.

A gating functionality can be included in the current therapy concept with moderate effort. However, any motion within the position window will remain unaccounted and lead in combination with a dynamic beam delivery to dose inhomogeneities. Any reduction of the position window will automatically elongate the treatment time. Due to this disadvantage gating was excluded from the current study.

The general applicability of rescanning in heavy ion therapy was theoretically and experimentally investigated in this thesis. Averaged over a large number of sub-fractions (N), the homogeneity of the dose distribution to a moving target improved in a limited part of the irradiation field under certain conditions approximately with $\frac{1}{\sqrt{N}}$. The border region, however, remained strongly inhomogeneous. To deposit a

homogeneous dose in all parts of the target volume, the field has to be extended, increasing the amount of dose deposited in the normal tissue, compared to the static case. Moreover, depending on the time correlation between scanning and target motion, large inhomogeneities can remain in the integral dose distribution. The active beam delivery of magnetic raster scanning strongly suggests dynamic beam realignment, which was put into realisation in the framework of the current thesis. Simulations showed that 3D online motion compensation (3D-OMC) based on real-time beam realignment could deliver almost identical dose distributions to static and to moving target volumes. The strong dependence of the resulting dose distribution on amplitude, phase and frequency of the motion is eliminated by determining the actual displacement of the target voxel at the time of its irradiation and compensating the beam position accordingly.

Based on the simulations, a prototype setup was designed and assembled, modifying the settings of the scanning system during the irradiation to follow arbitrary motion patterns in three dimensions with the beam. The lateral motion compensation was achieved by a modification of the existing magnetic raster scanning system. In contrast to photon therapy, the depth compensation has to be fully included for ion irradiations, due to the pronounced dose enhancement in the Bragg peak region. Real-time energy variation in the accelerator was not possible. To perform a variation of the penetration depth independent of the time structure of the accelerator a fast, passive energy modulator, consisting of a movable wedge system mounted on a linear motor, was used.

The feasibility of the prototype setup was tested in different experiments assuming respiration-like target motion. The beam position was automatically adapted to the mechanically measured, real-time motion information. It was shown that the prototype setup compensated for any target motion with sub-millimetre precision. The application to complex, extended target volumes showed a similar precision. In this case the correct dose distribution optimised for a static target was delivered with an average precision of 1-2% to moving target volumes without elongation of the irradiation time or additional dose contribution to the surrounding volumes. These results provide a first step towards motion adapted heavy ion therapy which could extend the precision of heavy ion irradiation to moving tumour sites in thorax and abdomen. Problem definitions and possible solutions for motion adapted heavy ion therapy were discussed in this thesis. Further studies on treatment planning for dynamic target sites and real-time tracking of internal motion are already in progress.

Aiming at a clinical applicability, further experiments have to prove the correct interplay between longitudinal and lateral motion compensation. Suitable motion phantoms and an independent, video-based tracking system are under construction. In addition, a full integration of 3D-OMC into the scanning control and safety system is essential, enabling status logging of the compensation process and consistent data transfer within the control system. At the same time, the time correlation

between scanning and target motion can be measured precisely, eliminating the remaining uncertainty in the current simulations.

Zusammenfassung und Ausblick

Das Ziel der vorliegenden Arbeit bestand in der Untersuchung von geeigneten Methoden zur Bestrahlung bewegter Zielvolumina mit dem an der GSI verwendeten Rasterverfahren.

Das magnetische Rasterverfahren ermöglicht eine exzellente Anpassung der applizierten Dosisverteilung an das Zielvolumen, unter der Voraussetzung, dass sich dessen Lage relativ zum Bezugspunkt des Scanners nicht verändert. Steile laterale und distale Dosisgradienten ermöglichen eine Bestrahlung mit hoher Dosis in der direkten Nähe von Risikoorganen.

Intensitäts-modulierte Ionentherapie ist deutlich sensitiver auf Bewegungen des Zielgebietes als andere Präzisionsstrahlentherapieformen (z. B. IMRT), die jedoch grundsätzlich der gleichen Problematik unterliegen. In der Praxis wird eine Ruhigstellung des Zielgebietes mittels stereotaktischer Fixierung von knöchernen Strukturen vorgenommen. Dieser Ansatz ist beim Auftreten von inneren Bewegungen relativ zu den starren Strukturen (z. B. durch Atembewegungen) nicht anwendbar. In diesem Fall zerstört die Interferenz zwischen der dynamischen Bestrahlung und der Zielgebietsbewegung die Volumenkonformität und weicht die steilen Dosisgradienten auf. Innerhalb des Zielgebietes entstehen dabei Stellen mit Über- und Unterdosierung, die den Therapieerfolg in Frage stellen.

Aus den Untersuchungen für andere Strahlentherapieformen haben sich im wesentlichen drei Lösungsansätze für die Bestrahlung bewegter Zielgebiete herauskristallisiert: eine kontrollierte Unterbrechung der Bestrahlung sobald das Zielvolumen sich außerhalb eines vordefinierten Positionsfensters befindet (Gating), eine Mittelung der Dosisabweichungen über mehrere zur Bewegung unkorrelierte Teilbestrahlungen mit reduzierter Dosis (Rescanning) und eine aktive Nachverfolgung des aktuellen Zielpunktes mit dem Therapiestrahler.

Gating lässt sich im bestehenden Konzept mit moderatem Aufwand realisieren. Innerhalb des Positionsfensters wird allerdings jede Bewegung akzeptiert, ohne in der Bestrahlung besonders berücksichtigt zu werden. Bei dynamischer Bestrahlung mit einem feinen Strahl entstehen dabei, je nach Größe des Positionsfensters, starke Dosisinhomogenitäten. Eine Verkleinerung des Positionsfensters führt jedoch unweigerlich zu einer Verlängerung der Bestrahlungsdauer. Aufgrund dieses Nachteils wurde Gating im Rahmen dieser Arbeit zunächst ausgeschlossen.

Die prinzipielle Verwendbarkeit der Mehrfachbestrahlung in der Schwerionentherapie wurde theoretisch und experimentell untersucht. Durch eine Mittelung über viele Teilbestrahlungen (N) wurde in einem begrenzten Bereich des Bestrahlungsfeldes unter bestimmten Bedingungen eine Verbesserung der Dosisinhomogenität mit

$\frac{1}{\sqrt{N}}$ beobachtet. Der Randbereich blieb jedoch stark inhomogen. Um eine homogene Dosisverteilung über das gesamte Zielvolumen zu erzielen, muss das Bestrahlungsfeld erweitert werden, wodurch zwangsläufig mehr Dosis in den Bereichen außerhalb des eigentlichen Zielgebietes deponiert wird als im statischen Fall. Außerdem können, je nach zeitlicher Korrelation zwischen Strahl- und Zielgebietenbewegung, deutliche Strukturen in der integralen Dosisverteilung auftreten.

Die aktive Strahlführung des magnetischen Rasterverfahrens legt eine aktive Nachführung der Strahlposition während der Bestrahlung nahe, die im Rahmen der vorliegenden Arbeit realisiert wurde. Anhand von Simulationen wurde gezeigt, dass mit einer drei-dimensionalen Korrektur der Strahlposition in Echtzeit nahezu identische Dosisverteilungen an bewegte, wie statische Zielgebiete abgegeben werden können. Die starke Abhängigkeit der applizierten Dosisverteilung von Amplitude, Phase und Frequenz der Bewegung wird dadurch eliminiert, dass zum Zeitpunkt der Bestrahlung die Verschiebung des Zielpunktes relativ zur Sollposition bestimmt und die Strahllage entsprechend angepasst wird.

Basierend auf den vorgestellten Simulationen wurde ein Prototyp System entwickelt und aufgebaut, welches die Einstellungen des Scannersystems zur Laufzeit derart veränderte, dass der Strahl in allen drei Raumrichtungen einer beliebigen Zielgebietenbewegung nachgeführt werden konnte. Eine Erweiterung des bestehenden Rasterverfahrens ermöglichte die laterale Bewegungskorrektur. Besonderes Augenmerk galt jedoch der Tiefenkorrektur. Im Gegensatz zur Photonentherapie muss, aufgrund der ausgeprägten Dosisüberhöhung im Bereich des Bragg-Peaks, die Tiefeninformation in der Ionentherapie vollständig berücksichtigt werden. Da die Möglichkeit einer aktiven Energieänderung der Ionen während des Beschleunigungszyklusses nicht bestand, wurde ein schneller, passiver Energiemodulator, bestehend aus einem beweglichen Doppelkeilsystem auf Linearmotoren, eingesetzt.

Die Funktionalität des Prototyp Systems wurde in verschiedenen Experimenten für atmungsähnliche Bewegungen getestet. Die Bewegungsinformation wurde dabei in Echtzeit mechanisch erfasst und die Strahllage vom System automatisch angepasst. Es konnte gezeigt werden, dass der Prototyp Aufbau in der Lage war, Zielbewegungen mit einer Genauigkeit von weniger als einem Millimeter zu kompensieren. Die Anwendbarkeit auf komplexe, ausgedehnte Zielgebiete konnte mit vergleichbarer Präzision gezeigt werden. Dabei wurde die für den statischen Fall geplante Dosisverteilung ohne zeitlichen Mehraufwand oder zusätzliche Belastung umliegender Volumina mit einer Genauigkeit von 1-2% an bewegte Zielgebiete appliziert.

Diese Ergebnisse stellen einen ersten Schritt in Richtung einer bewegungsmodulierten Schwerionentherapie dar, welche die Bestrahlung von Tumoren im Thorax- und Abdomenbereich mit der Präzision von Schwerionenstrahlen ermöglichen würde. Bezüglich dieser Anwendung wurden Problemanalysen durchgeführt und Lösungsansätze diskutiert. Weitere Studien zur bewegungsmodulierten Bestrahlungsplanung und zeitaufgelösten Erfassung von Organbewegungen werden bereits durchgeführt.

Im Hinblick auf eine klinische Anwendbarkeit sind noch weitere Studien notwendig. Insbesondere muss das Zusammenspiel von lateraler und longitudinaler Bewegungskompensation experimentell nachgewiesen werden. Dazu erforderliche Bestrahlungsphantome, sowie ein unabhängiges, optisches System zur Bewegungserfassung in Echtzeit befinden sich in Vorbereitung. Aussenden ist eine vollständige Integration in das Therapiekontrollsystem zur Funktionsüberwachung und zum konsistenten Austausch von Daten innerhalb des Systems erforderlich. Gleichzeitig könnte auch die Zeitkorrelation zwischen Bestrahlung und Zielgebietenbewegung, der verbleibenden Unsicherheit in den Simulationsrechnungen, erfasst werden.

Appendix A

Terms and Terminology

A.1 Geometrical Concepts in Radiation Cancer Therapy

According to the specifications of the International Commission on Radiation Units and Measurement (ICRU) [ICR93, ICR99] several types of subvolumes have to be considered when defining the target volume.

The palpable or by any means visible extension of the malignant growth defines the *Gross Target Volume (GTV)*. This volume is extended by a margin for subclinical, microscopic spread of malignant disease which is not visible but has to be treated the same way as the cells in the GTV. The combination of both subvolumes defines the *Clinical Target Volume (CTV)* as the purely anatomical-clinical region which has to be treated.

Depending on the treatment technique used, additional margins have to be added which ensure that the CTV really receives the prescribed dose. The resulting

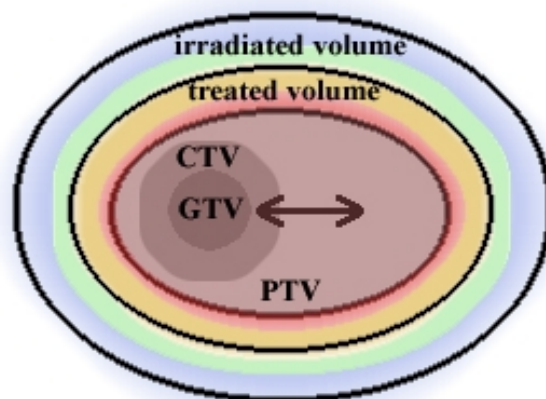


Figure A.1:

Illustration of the geometrical concepts for target volume definition used in cancer therapy. The different target volumes are drawn in gray scale, superimposed by a colour-coded dose distribution (all schematically).

Planning Target Volume (PTV) includes the CTV and a margin which accounts for any geometrical variation and inaccuracy of the planned irradiation. Its size strongly depends on the treatment modalities. Examples for variations which lead to an enlarged PTV are: inaccuracies in patient positioning, day-to-day variations in the shape, volume and position of the organs (e.g. bladder) and any intra-fractional motion of the patient and/or the organs. If for instance the CTV will be subject to an uncompensated organ motion, the PTV has to be large enough to cover the maximum displacements guaranteeing that every point of the CTV is permanently inside the radiation field. The PTV is the basis for treatment planning and is referred to as *target volume* in this thesis.

Two further subvolumes are important for discussing the quality of the treatment modality: The *treated volume* is enclosed by an isodose surface appropriate to achieve the purpose of the treatment and the *irradiated volume* includes all tissue that has received a significant dose compared to normal tissue tolerance.

A.2 Anatomical Directions and Planes

The following section will summarise the anatomical terms and definitions relevant for this thesis. For more details refer to [Don02]. All definitions are based on the so called *standard anatomical position*: standing, feet together, palms forward, looking forward. In this position a human body has four orthogonal planes of reference (see fig. A.2):

- **transverse plane:** slices the body horizontally at any height, also called horizontal plane
- **sagittal plane:** divides the body into left and right halves, any slice parallel to the middle one is called parasagittal
- **coronal plane:** divides the body into anterior and posterior halves, also called frontal plane
- **oblique plane:** lies at any other angle

To express the position of two objects relative to each other the following pairs of terms are used:

- **superior – inferior:** above – below
- **anterior – posterior:** in front of – behind
- **medial – lateral:** closer to – further away from mid-line

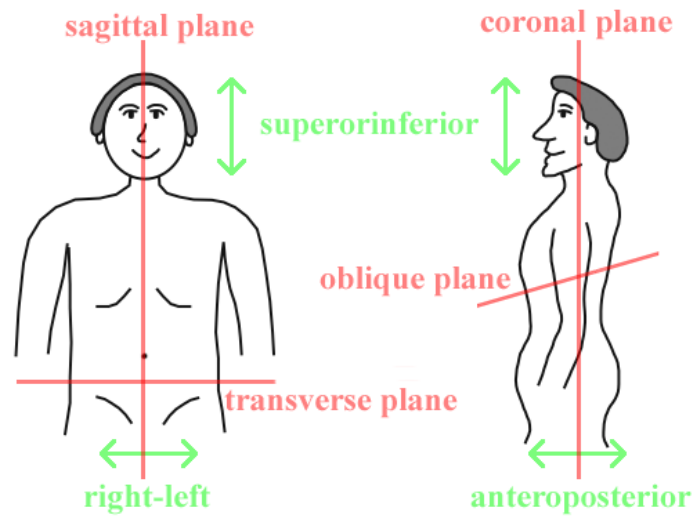


Figure A.2: Anatomical planes and directions

For each of these terms at least one synonymous exists. Superior is equivalent to **cranial**, inferior to **caudal**, anterior to **ventral** and posterior to **dorsal**. The terms medial and lateral cannot be literally replaced since they only express a direction with respect to the mid-line of the body. However, the use of left and right leads to the same meaning. Combinations of two relative positions describe directions of motion, view etc. Terms like **anteroposterior**, **superoinferior** or **right-left** are formed. In principle these expressions point into one direction. However in this thesis they represent a "bidirectional vector", describing a (cyclic) motion parallel **and** antiparallel to the pointing vector.

Appendix B

Estimation of Respiration-Related Target Rotation

In first, very coarse approximation, the lung can be replaced by half an ellipsoid. The three semi-major axes a, b, c represent the lung extensions in s. i., r. l. and a. p. directions, respectively. Their magnitude was determined under the following assumptions:

1. a total lung volume of 5.5 l (inhale)
2. a tidal volume of 0.5 l
3. a max. respiration-related motion of 12/5/5 mm
4. an optimum surface-to-volume ratio

Solving the elliptical volume

$$V = \frac{4}{3}\pi abc \quad (\text{B.1})$$

and surface

$$F(x, y, z) = \frac{x^2}{a^2} + \frac{y^2}{b^2} + \frac{z^2}{c^2} = 1 \quad (\text{B.2})$$

equations [Bro93] for these conditions yields: $a = c = 110$ mm and $b = 200$ mm. The resulting surfaces for the two extreme cases (inhalation and exhalation) are shown in fig. B.1(a).

At each surface point (\vec{x}_T) the tangent plane was determined:

$$\frac{\partial F}{\partial x}(x - x_T) + \frac{\partial F}{\partial y}(y - y_T) + \frac{\partial F}{\partial z}(z - z_T). \quad (\text{B.3})$$

In general, the angle between a straight line $(\vec{X} - \vec{x}_1) \times \vec{R} = 0$ and a plane $\vec{r}\vec{N} + \vec{D} = 0$ is calculated by [Bro93]:

$$\sin\phi = \frac{\vec{R}\vec{N}}{RN} \quad (\text{B.4})$$

This way, the intersection angles of these tangent planes with the three axes of the coordinate system were calculated. The target rotation components were taken

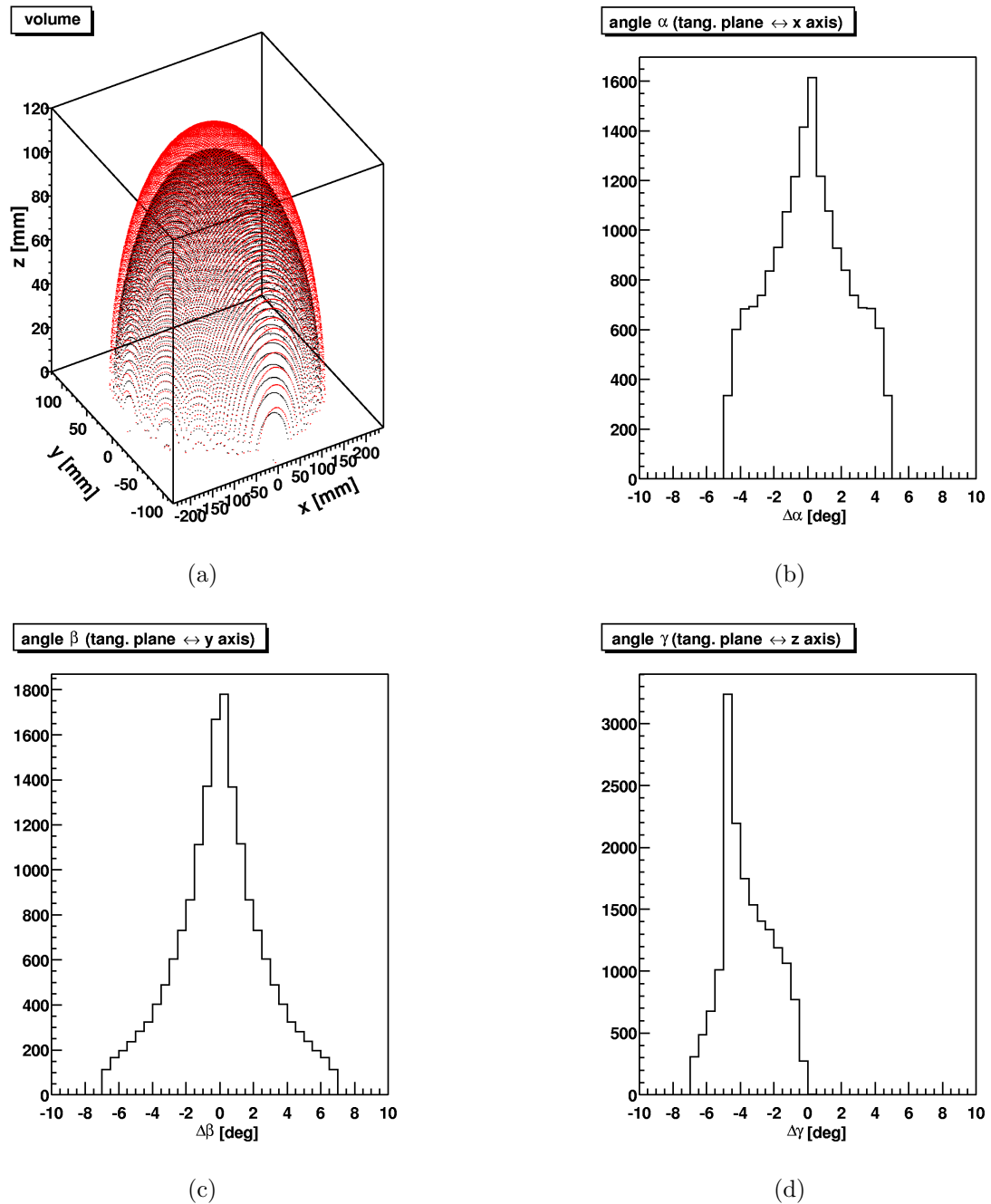


Figure B.1:

Estimation of the respiration-related rotation amplitude of a target volume attached to the lung. The lung is approximated by half an ellipsoid with variable volume (a). The rotation angle for each surface point is the difference in intersection angle with the three axes (b)-(d). In all three cases, the probability for a rotation by less than $\pm 5^\circ$ is more than 85%.

as the difference in the intersection angles between two states of motion \vec{x}_0 and $\vec{x}_0 + \Delta\vec{x}$:

$$\Delta\phi_i = \phi(\vec{x}_0) - \phi(\vec{x}_0 + \Delta\vec{x}) \quad (\text{B.5})$$

In fig. B.1(b)-B.1(d), the statistical distribution of the rotation angles is plotted for all surface points for the transition from inhalation to exhalation. The distributions are symmetrical in B.1(c) and B.1(b) because of the rotation symmetry of the ellipsoid with respect to the z-axis. Since the lung was approximated only by the upper half of the ellipsoid, the distribution in B.1(d) is biased. However, in all three cases the probability for a respiration-induced target rotation by less than $\pm 5^\circ$ is higher than 85%. Therefore, $\pm 5^\circ$ rotation around each axis is considered to be a feasible value for the investigations within this thesis.

Appendix C

Medical Imaging Methods

The following chapter provides a review on existing medical imaging techniques with respect to real-time tracking of organ motion. For more details refer to standard text books like [e. g. Lau86, Mor95].

C.1 X-ray imaging

The oldest and still most widely used imaging technique is radiography. This method exploits the different absorption cross-sections of x-rays in internal structures (bone, muscle, lung etc.). The x-rays are generated in an x-ray tube as bremsstrahlung from electrons which have previously been accelerated in an electric field (see fig. C.1). As discussed in chapter 2.1 a beam of electromagnetic radiation is exponentially attenuated according to eq. (2.3), when penetrating matter. Every material has its characteristic absorption coefficient μ . The attenuation

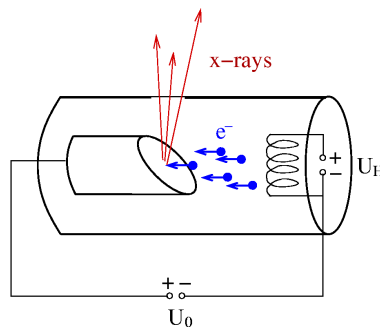


Figure C.1:

The generation of x-rays in an x-ray tube is based on bremsstrahlungs processes. Electrons emitted by a filament are accelerated towards the anode by a voltage U_0 . When hitting the anode a fraction of their energy is converted into x-rays which are focussed on the exit window by the specific shape of the anode.

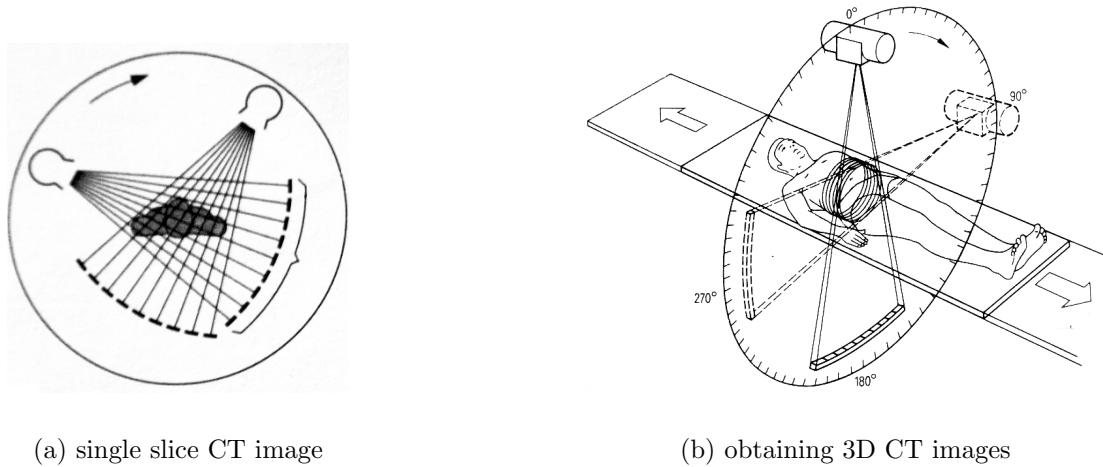
along the beam is described by the line-integral over all attenuation coefficients [Mor95]

$$p = \int_s \mu(x, y, z) ds \quad (\text{C.1})$$

As radiographs show the projection of x-ray absorption along the beam, they provide a planar view of all structures overlapping each other. Consequently, no direct 3-dimensional information can be extracted from radiographs. Especially out-of-plane rotations are not evident [e. g. Rem00]. However, comparing the planar images to a 3D reference, an exact position verification is possible. The latter strategy is used, for instance, for patient positioning in radiation therapy (cf. chapter 2.4.2). The transmission of the x-rays after having penetrated the body is recorded either on radiographic films or digitally with image amplifiers. The quality of the images depends on two major factors: the focussing of the beam and the energy of the photons. The contrast of the radiographs has to be optimised for the specific situation. In general, a higher contrast leads to a larger dose deposition (lower energy beams deposit more energy inside the body). For dedicated examinations, a contrast agent can be applied increasing the x-ray absorption in certain organs. One of the most critical problems for real-time image analysis is the pattern recognition. The overlapping of different shapes with variable contrast requires prominent structures to be defined which can easily be recognised. One solution is the use of fiducial markers, i. e. small metal balls or flags, which are (endoscopically) attached to the site of interest and can clearly be seen on the images. The corresponding spots on the radiographs can be detected very fast by a pattern recognition software, even on images with a generally low contrast. In addition, using two or three sets of orthogonal radiographs, the relative orientation of multiple markers can be used to extract the motion of the organ they are attached to with a precision of better than 1 mm and 1° [Bal95].

C.2 Computed Tomography (CT)

Full 3D x-ray images of the body are taken in computed tomography (CT). According to eq. (C.1) the attenuation of an x-ray beam along a straight line through the body is measured in radiography. To obtain 3D images, the attenuation has to be measured from many directions. From the crossing rays, the attenuation for every single point in a slice can be determined by inverse projection. Fig. C.2(a) shows an example of a fanbeam CT in which the x-rays from a single source penetrate the body like a fan. A multiarray detector behind the patient measures the intensity of every ray. To obtain signals from many directions, the source and detector are rotating around the patient. For a 3D data set the patient is moved through the CT scanner either from slice to slice or in a continuous motion (spiral CT).



(a) single slice CT image

(b) obtaining 3D CT images

Figure C.2:

These figures illustrate how to obtain a 3D CT data set considering a fanbeam CT as example (figures taken from [Mor95]). (a) The x-rays from a single source penetrate the patient like a fan. A multiarray detector measures the attenuation for each ray. To obtain signals from many directions the setup is rotating around the patient. From the crossing line integrals at a certain point, the attenuation can be determined via inverse projection algorithms. (b) Several parallel slices are stacked to a 3D image. The slices are measured by moving the patient couch through the CT scanner.

Revealing the electron density inside the patient, CT imaging is essential for treatment planning in particle therapy. The use of CT for real-time tracking would eliminate the need for a correlation of the motion data to the time-resolved planning data sets. Cause for concern is raised only by the dose deposition to the patient. The large amount of pencil-like x-ray beams, required for a 3D CT image, accumulate a large dose in the patient. In average, a dose of 10 mSv is applied in a single conventional CT scan of the thorax [Bun00]. With modern ultrafast CT scanners an imaging rate of about 4 Hz [e. g. Ros90], for limited volume sizes even up to 38 Hz¹, can be achieved. Integrated over the whole treatment (4-5 min per field, 2-3 fields on 20 consecutive days), the diagnostic contribution would be of the same order of magnitude as the therapeutic dose. With lower image frequency and spatial resolution the radiation exposure can be reduced by up to 94% [Car01]. However, one limitation for the use in heavy ion therapy remains: A CT scanner is a too bulky device to be operated in parallel to the PET camera during a heavy ion irradiation.

¹According to the product information of Phillips Mx8000IDT, 16 simultaneous slices can be acquired with speeds up to 38 images per second (Philips Medical Systems, Best, Netherlands).

C.3 Nuclear Medicine

In contrast to x-ray imaging, which measures the interaction of externally applied radiation with matter, nuclear medicine exploits the radioactive decay of atoms inside the body. These are small amounts of radioactive substances (radio-isotopes), injected into a patient to trace disease processes. In most cases, the radio-isotopes are attached to carrier molecules, which accumulate in a certain tissue or are involved in the disease process. Today, for each organ a specific radioactive compound exists to examine its functions with nuclear medicine techniques. Consequently, the strength of nuclear medical imaging is the visualisation of dynamic processes (metabolism, blood flow etc.). The radio-isotopes decay after a life-time, which has been optimised to the imaging process and (directly or as secondary products) emit one or more photons. These photons penetrate the body and are detected by gamma cameras positioned close to the patient.

The two main nuclear medical imaging methods are positron emission tomography (PET) and single photon emission computed tomography (SPECT). PET relies on the characteristics of β^+ decays ($p \rightarrow n + e^+ + \nu_e$), i. e. on the fact that the emitted positron will mostly annihilate after a very short distance (few mm) into two oppositely directed 511 keV γ -quanta. The annihilation quanta are emitted under an angle of exactly 180° to each other in the rest frame. If these two γ -quanta are measured in coincidence by two opposing detectors (scintillation crystals) outside of the body, the decay happened somewhere along the intersection line (see fig. C.3). From the superposition of many of these lines at different angles the origin of the β^+ activity can be reconstructed.

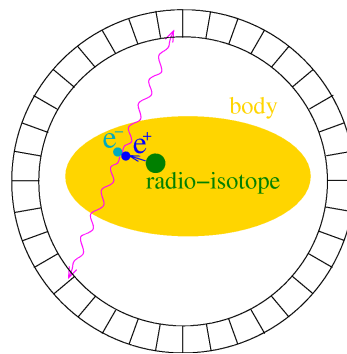


Figure C.3:

Principle of PET measurements: A radio-isotope (either radioactively marked tracer or fragments from a therapy beam) decays via positron emission. This positron travels up to a few mm until it annihilates with a tissue electron. The two 511 keV, back-to-back oriented annihilation quanta are detected in coincidence in a ring of scintillators positioned around the patient.

The spatial resolution of a PET scanner is dominated by the properties of the single detector crystals. Physically, the spatial resolution of a full body PET image is limited to about 2-3 mm [Mor95]. Considering that the respiration-related a.p. and r.l. displacement is typically as small as $\pm 4-5$ mm (see chapter 3.2), this resolution is definitely not sufficient for online motion tracking in motion adapted heavy ion therapy. Moreover, one of the major challenges in using PET for online treatment verification, is the low signal-to-noise ratio. Tracking the tumour position with PET would require the target tissue to be marked with suitable radio-isotopes. In this case the strength of the tracer signal would interfere with the weak, beam-induced signal, which has to be measured in parallel.

SPECT works quite similar as PET, despite the fact that it measures single photon emission, while PET detects the annihilation photons of the positrons with the target electrons in coincidence. Due to the missing coincidence condition, a collimator is required to determine the position of decay. In general, SPECT has a spatial resolution, which is for each dimension by a factor of 2-4 lower than for an optimised PET [Mor95].

C.4 Magnetic Resonance Imaging (MRI)

Magnetic resonance imaging (MRI) is based on the physical phenomenon of nuclear magnetic resonance (NMR). Every nucleus with an odd number of protons or neutrons possesses a spin I , acting like a dipole with a magnetic moment $\vec{\mu}_I$ proportional to the nuclear gyromagnetic ratio γ_I

$$\vec{\mu}_I = \gamma_I \hbar \vec{I} \quad (\text{C.2})$$

When brought into an external magnetic field this dipole has a potential energy proportional to the magnetic flux \vec{B}

$$W = -\vec{\mu}_I \cdot \vec{B} \quad (\text{C.3})$$

The spin has $2I+1$ different options to align to the magnetic field ($-I \leq m_I \leq +I$), resulting in the same number of discrete energy levels proportional to the Larmor frequency ω_L

$$\hbar\omega_L = E_{m-1} - E_m = \gamma_I \hbar B_0 \quad (\text{C.4})$$

In MRI, a resonant excitation of the tissue with an optimised HF-pulse alters the orientation of the spin relative to the external magnetic field. In practice, a so called 90° -pulse aligns the spins orthogonal to the base field. When the HF is switched off the spin realigns to the static magnetic field inducing a time varying signal in an HF receiver coil. This signal can be analysed according to two characteristics: the intensity of the signal which is proportional to the proton density and the relaxation time providing information about the mobility of the nuclei. The relaxation time

has two components: the longitudinal relaxation time T_1 , measuring the time in which the magnetisation parallel to the base field is restored, and the transversal time T_2 , referring to the orthogonal orientation. While the longitudinal relaxation is determined by the energy transfer to the lattice the atom is integrated into, the transversal component is dependent on the interaction of the spins among each other.

MRI is perfectly suited to image soft tissue and provides vital information for tissue delineation in treatment planning. Some typical longitudinal relaxation times of healthy and malignant tissues are given in tab. C.1 illustrating the differences in the measured signal. However it is not feasible for the online use in heavy ion

| tissue | longitudinal relaxation time T_1 [s] | |
|------------------|--|-----------------|
| | normal | tumourous |
| mamma | 0.37 ± 0.08 | 1.08 ± 0.08 |
| skin | 0.62 ± 0.02 | 1.05 ± 0.11 |
| muscle | 1.02 ± 0.03 | 1.41 ± 0.03 |
| liver | 0.57 ± 0.03 | 0.83 ± 0.01 |
| stomach | 0.77 ± 0.08 | 1.24 ± 0.11 |
| lung | 0.79 ± 0.06 | 1.10 ± 0.06 |
| bone | 0.55 ± 0.03 | 1.03 ± 0.15 |
| spleen | 0.70 ± 0.05 | 1.11 ± 0.11 |
| fat | ≈ 0.2 | |
| H ₂ O | 3.6 | |

Table C.1:

Typical values for longitudinal relaxation times T_1 of human tissue (taken from [Lau86]).

therapy, since the magnetic fields will deflect the charged particles and thus make a controlled beam delivery impossible. Ions with momentum p and charge q traversing a magnetic field with a flux B are deflected on a circular track with radius ρ

$$\rho = \frac{p}{qB} \quad (\text{C.5})$$

For small deflection angles (short travelling distance s parallel to the initial direction) the lateral deflection Δ can be derived from purely geometrical considerations

$$\Delta \approx \rho \left(1 - \sqrt{1 - \frac{s^2}{\rho^2}} \right) \quad (\text{C.6})$$

Following eq. (C.5) and (C.6) ^{12}C ions with therapeutically relevant energies of $85 \frac{\text{MeV}}{\text{u}}$ and $430 \frac{\text{MeV}}{\text{u}}$ are laterally deflected by 1.9 mm and 0.8 mm respectively when

travelling a distance of 0.1 m through a typical NMR base field of 1 T. The lateral deflection is of the order of the voxel dimensions and thus intolerably large. In addition, the base field of a NMR scanner is usually shaped inhomogeneously to get a high spatial resolution in 3D. This would lead to a non-constant deflection pattern for ions with the same energy.

C.5 Ultrasound Imaging

Ultrasound (US) imaging, also called sonography, originates from the tracking of submarines in the Second World War. In the pulse echo technique a short, high frequency ultrasound pulse (medical US imaging: 1 MHz - 15 MHz) is emitted into the matter to be scanned (water, tissue etc.). From its reflection pattern the information on the density distribution can be extracted.

Sound waves are periodical mechanical distortions of the state of equilibrium of matter which propagate in space. The propagation requires the presence of elastic matter. In gases, liquids and biological tissue, only longitudinal waves occur. Starting with the 3D wave equation

$$\frac{d^2\xi}{dt^2} = c^2 \left(\frac{d^2\xi}{dx^2} + \frac{d^2\xi}{dy^2} + \frac{d^2\xi}{dz^2} \right) \quad (\text{C.7})$$

with the three-dimensional wave vector ξ and Hook's law

$$p = K\xi \quad (\text{C.8})$$

as the equation of state for elastic media, one yields a sound velocity c which depends on the mass density ρ and the bulk modulus K of the propagation medium

$$c = \sqrt{\frac{K}{\rho}}. \quad (\text{C.9})$$

The product of mass density ρ and sound velocity c is called sound impedance Z

$$Z = \rho c \quad (\text{C.10})$$

and purely depends on the properties of the material. A sound wave which penetrates matter is partially reflected if the sound impedance changes. The reflection coefficient is proportional to the difference in sound impedances

$$R = \left(\frac{Z_1 - Z_2}{Z_1 + Z_2} \right)^2. \quad (\text{C.11})$$

Typical values for biological relevant materials are given in tab. C.2.

| material | sound velocity c m/s | mass density ρ g/cm ³ | reflection coefficient R against H ₂ O |
|----------------|---------------------------|--|--|
| air | 330 | 0.0012 | 0.999 |
| adipose tissue | 1400 | 0.928 | 0.042 |
| water | 1490 | 0.997 | 0 |
| liver | 1560 | 1.055 | 0.054 |
| muscle | 1568 | 1.058 | 0.054 |
| bone | 3360 | 1.58 | 0.614 |

Table C.2:

Typical values for sound velocity in biological material (taken from [Lau86]).

In general, all wave phenomena known from the optics of light, like scattering, refraction, diffraction etc., influence the amount of sound being reflected back to the point of origin. The largest fraction of the signal actually comes from back-scattering processes on tilted surfaces. Since these processes are not essential to understand the main principle of US imaging, the reader is referred to standard text books [e. g. Mor95]. However, a detailed analysis of these processes is important when dealing with imaging artefacts.

In US imaging devices, the ultrasound wave is generated and received by the same transducer (sonic head). The generation is based on the inverted piezoelectrical effect. Certain crystals are deformed by applying a high frequency alternating current, tuned to the mechanical eigenfrequency. This deformation is transformed into ultrasonic waves. With the same crystal, the reflected wave can be measured. The ultrasound wave causes a deformation of the crystal structure which produces an electrical current on the surface, basically due to charge displacement (piezoelectrical effect). The distance z of the discontinuity in sound impedance from the transducer is determined by the time difference t between emission of the imaging pulse and the arrival of the echo signal

$$z = \frac{ct}{2}. \quad (\text{C.12})$$

At the same time, the amplitude of the signal is a measure for the amount of reflection, i. e. the properties of the tissue boundaries.

The spatial resolution parallel to the beam is given by the minimum distance of two echos

$$\Delta z = \frac{c\Delta t}{2} > \frac{c}{2\nu} = \frac{\lambda}{2}. \quad (\text{C.13})$$

and a shorter wavelength leads to a better spatial resolution. On the other hand, like any electro-magnetic wave, the US beam is attenuated exponentially when

penetrating matter (cf. eq. (2.3)). In biological tissues the absorption coefficient is in first approximation proportional to the frequency of the wave [Mor95] and a long US wavelength is required when imaging deep seated structures. Consequently, the choice of US frequency will always be a compromise between imaging depth and spatial resolution, requiring the experience of the examiner. Typical values for the imaging depth and spatial resolution are given in tab. C.3. The lateral resolution is proportional to the inverse of the width of the imaging beam, which depends on the frequency and the dimensions of the crystal [Lau86]. An US beam with a maximum, bidirectional penetration depth of 10 cm already has a lateral resolution of more than 1 mm.

| emitting frequency MHz | wavelength mm | penetration depth (bidirectional) cm | lateral resolution mm | longitudinal resolution mm |
|------------------------------|------------------|--|-----------------------------|----------------------------------|
| 2 | 0.78 | 25 | 3 | 0.8 |
| 3.5 | 0.44 | 14 | 1.7 | 0.5 |
| 5 | 0.31 | 10 | 1.2 | 0.35 |
| 7.5 | 0.21 | 6.7 | 0.8 | 0.25 |
| 10 | 0.16 | 5 | 0.6 | 0.2 |
| 15 | 0.1 | 3.3 | 0.4 | 0.15 |

Table C.3:

Typical parameters for diagnostic ultrasound imaging (taken from [Mor95]).

The measured data can be visualised by different methods. The easiest way is to plot the amplitude of the signal vs. the arrival time. This imaging method is known as the *A-image* (amplitude). The more common type of visualisation is the *B-image* (brightness). Here, the sonic beam is shifted in the plane orthogonal to the beam after each pulse. On the screen a 2D image is plotted, with the beam position in horizontal and the echo time in vertical direction. The amplitude of the signal determines the brightness of the corresponding pixel. The principle of B-image acquisition is schematically shown in fig. C.4. A third visualisation method is the *M-mode*. In this case, the beam is not swept but held at a fixed position over the tissue. The echo signal is plotted vs. the time. This presentation is extremely useful to visualise the motion of typical structure but does not provide any 3D information.

In former times, the sonic head was moved manually to get a B-image. This technique is known as *Compound Scan*. Nowadays, electronic or mechanical heads are used, which sweep the imaging area automatically. According to the scanning pattern these are grouped into linear (parallel), convex and sector scanners. In case of the first two, the effective transducer is shifted sideways, whereas in the latter case

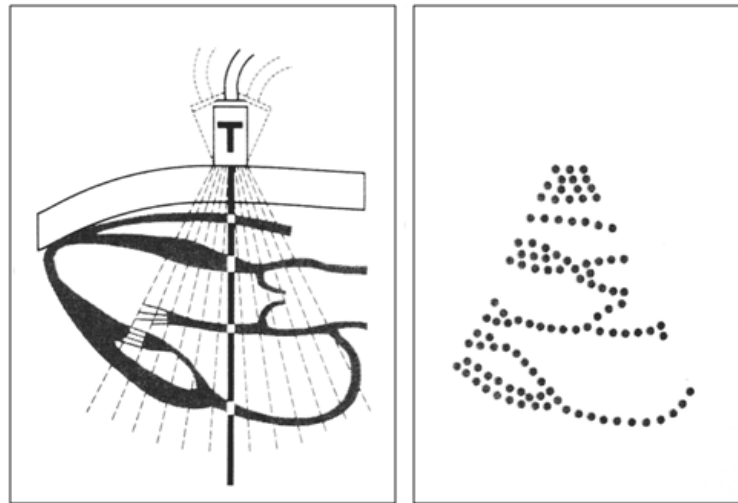


Figure C.4:

Principle of B-image acquisition of the heart (taken from [Mor95]). Rotating the transducer the sonic beam is swept orthogonal to its direction of propagation (left figure). The echos are plotted in a 2D image (B-image, right figure) with the beam position in horizontal and the echo time in vertical direction. The amplitude of the signal determines the greyscale value of the pixels.

it is rotated. In any case, the transducer has to remain at the same position long enough to receive the last echo. This time is determined by the imaging depth Z

$$dT = \frac{2Z}{c}. \quad (\text{C.14})$$

The maximum rate of 2D images depends on dT and the number of sweeping positions.

Following the same principle, 3D images of a whole volume can be taken. If the transducer is shifted or rotated in the plane orthogonal to the 2D image as well, several 2D images are stacked to monitor a 3D volume. The imaging rate is reduced by the number of single 2D images.

In addition, the Doppler shift of the sonic wave can be used to extract the velocity of the motion parallel to the imaging beam. Doppler sonography is routinely used for instance to study the physiology of the cardiovascular system.

Appendix D

Construction of PMMA Wedges

The prototype setup for 3D online motion compensation, described in chapter 5, combines the magnetic scanning system for lateral beam deflection and a dynamic wedge drive for fast energy modulation. The principle of passive energy modulation with dynamic PMMA wedges was already successfully used for depth scanning [Web00]. In contrast to the magnetic raster scan technique, a fixed beam was longitudinally scanned through the target volume by passive energy modulation and the stacking of the resulting cylinders to a 3D conformal volume was achieved by repositioning the target. The fast, passive energy modulation was achieved with a double PMMA wedge system mounted on two linear motors [GSI99]. The beam passes through the region of overlapping tips. By moving the wedges relative to each other, the amount of overlap and thus the energy deposition in the wedge material is adapted. The depth scanning application does not require a large active area¹ of the wedge drive.

In case of active beam scanning, the centre of the wedge drive, where the PMMA thickness is well defined, has to follow the beam. While the absolute wedge position can be adapted by the wedge drive control system to match the horizontal beam position, a vertical shift is not possible. Therefore, the height of the wedges has to cover all allowed beam positions. This made a re-design of the wedges, originally used for depth-scanning, necessary. While the characteristics (steepness, thickness, length etc.) were kept unchanged, the height of the standing wedges was extended to 15 cm. This value provided a compromise between covering the full field of the scanner (20 cm) and the weight of the wedges. The more load on the wedge drive, the slower is the acceleration. Since a high performance of the drive is required, even for the slow scanning direction parallel to the drive, the wedges were not extended further than 15 cm. In addition, a larger height of the free-standing wedges would have led to an oscillation of the wedge top at high drive acceleration.

The properties of the wedge drive are derived from the material properties of PMMA and the geometrical dimensions of the wedges. PMMA has a mass density of

¹Active area refers to the overlap area of defined thickness in the middle of the wedge drive system.

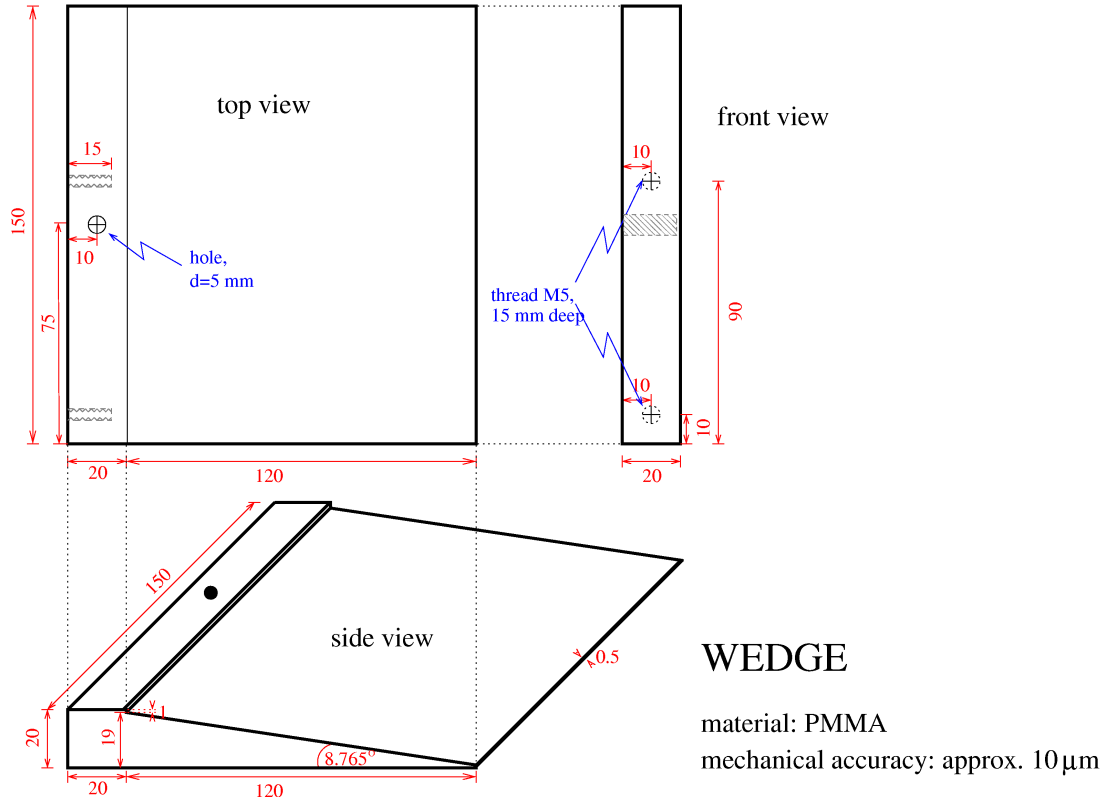


Figure D.1:

Construction plan for the PMMA wedges of the fast range modulator.

$\rho = 1.18 \pm 0.02 \frac{\text{g}}{\text{cm}^3}$. The density conversion factor from PMMA to water is 1.165 [Jac97]. Consequently, 1 mm PMMA corresponds to 1.165 mm water:

$$x(\text{PMMA}) = \frac{1}{1.165}x(\text{H}_2\text{O}) \quad (\text{D.1})$$

Due to purely geometrical considerations, each mm shift in wedge position changes the thickness of a single wedge by 0.1542 mm. For two blocks of five wedges each the resulting change in PMMA equals to 1.542 mm. That corresponds to a change of 1.80 mm in WE thickness. The wedges have an active area of 120 mm. With the reference position in the middle of this distance and a safety margin of 5 mm at each side, the maximum compensation capability of the wedge drive system amounts to ± 49.40 mm WEL. In the reference position the wedge drive system introduces a calculated WE thickness of 56.80 mm.

Appendix E

Software for the Prototype Setup

E.1 SAM Programs for Motion Compensation

This section documents the changes to the SCU software which had been necessary to include an externally measured, lateral displacement into the fast position correction of the existing active beam delivery system. The strategy of feeding the offsets into the SCU is discussed in more detail in chapter 5.2.2. For a detailed description of the scanning control system refer to chapter 2.4.1.

The seven control modules of the SCU run a module specific software. During the irradiation the measured data (e.g. beam position and intensity) is exchanged between the modules, checked for consistency and compared with the planned values. As soon as the data shows any inconsistency or too large deviations, an interlock is set. In the therapy mode, this leads to an immediate cutoff of the beam. Although, for safety reasons, a dedicated version of all the SAM software (`samXorg.c`) was created, only the software for the module, responsible for controlling the scanning magnets (SAMS), was adapted. Therefore, no consistency of the data among the different modules is given in the prototype setup. Each time SAMS realigns the beam to follow the moving target voxel, the motion-related shift is considered to be a deviation from the planned position by the other modules. Consequently, all measurements could only be performed in the experimental mode, where no interlocks are generated by deviations in beam position. The following changes in the source code are based on the file `sams_lf.c` dating from Dec. 2001. They serve as a guideline for a proper and consistent inclusion of the motion online compensation into the SCU.

line 42: declare variables for SMB access

```
    struct s_org {  int orgx;
                   int orgy;
                   int ctrl;
                   int wrx;
                   int wry;
    };
    volatile struct s_org *p_org;
```

line 96: declare and initialise displacement variables

```
int l_orgx=0, l_ory=0;
```

line 105: shift debugging information 10 bytes in SMB and place motion data into the first 10 bytes

```
p_deb = (struct s_deb *) (CRAM+0x10);
p_org = (volatile struct s_org *) CRAM;
```

line 144: has to be set later

```
/* l_state = MNG_SET; */
```

line 180: reset displacement values (safety)

```
p_org->orgx = 0;
p_org->orgy = 0;
p_org->ctrl = 0;
l_state = MNG_SET;
```

line 193: replace read-out by target to bypass interlock

```
l_readx = l_sollx;
l_ready = l_solly;
```

line 222: replace read-out by target to bypass interlock

```
l_istx = l_sollx;
l_isty = l_solly;
```

line 341: get actual beam position

```
l_orgx = l_sposx;
l_ory = l_sposy;
```

line 358: get actual beam position

```
l_orgx = l_sposx;
l_ory = l_sposy;
```

line 377: if SMB up-to-date, block SMB access, add offsets to target values and write sum back to SMB, finally pass sum to power supply

```
if(p_org->ctrl == 0x10)
{
    p_org->ctrl = 0x1;
    l_orgx = l_sposx + p_org->orgx;
    l_ory = l_sposy + p_org->orgy;
    p_org->wrx = l_orgx;
    p_org->wry = l_ory;
}
mng_corr(f_br, l_orgx, l_ory, l_iposx, l_iposy,
```

line 387: substitute target position by compensated one, enlarge active area of fast

```
position correction
if(abs(l_orgx - l_iposx) > 300)
    f_cx = 0.0;
if(abs(l_orgy - l_iposy) > 300)
    f_cy = 0.0;
```

line 392: substitute target position by compensated one

```
if(abs(l_orgx - l_iposx) < 10)
    f_xx = 0.3;
if(abs(l_orgy - l_iposy) < 10)
    f_yy = 0.3;
```

E.2 Wedge Drive Control System

As described in more detail in chapter 5.2.1 the wedge drive operating as fast energy modulator consists of a linear hybrid stepping motor and its electronics which are connected to a PC via a step and direction controller (AT6400). The drive is equipped with two linear encoders and three limit switches, one at each end of the linear rail and one connected to the slides preventing them from crashing together. The control system software runs in the LabView 6i environment under the operating system MS Windows95. The software itself currently consists of two components: the hardware control library *wedgedrive.llb* and the process control user interface *WD.llb*. Both components will be described in detail in this chapter. Apart from some test routines the *wedgedrive.llb* library contains the fundamental VIs (LabView routines) for controlling the stepping motor. The most important VIs are summarised in table E.1. In the current version, the wedge drive system has to be manually initialised before running the motion compensation interface. This is achieved with the two VIs *WDInitDrive95.vi* and *Home1.2.vi*. The flow diagram in fig. E.1 shows the sequence of VIs necessary to perform the longitudinal motion compensation.

The automatic compensation of the longitudinal target motion component is done by *WD.vi*. At the beginning the data client is started, setting up a TCP/IP connection to the E7. Via this connection the externally measured displacement information as well as the beam position are received. From both values the absolute position is calculated for each of the slides. Finally, the program determines the number of steps required for each axis (slide) and starts the motion. After the position is roughly reached, a feedback loop to the linear encoders guarantees the accurate positioning. During the positioning process the data client continuously receives new data. As soon as the transmitted data changes, the positioning of the wedges is cancelled and the new position is set. This way, no systematic offset can be built up as a result of potential drive latency.

| VI name | Description |
|------------------|--|
| Anzeige.vi | Displays the motor and encoder position of both axes and the status of the middle limit switch |
| Free-Mitte.vi | Moves each of the slides $500\ \mu\text{m}$ away from the other to clear the middle limit switch |
| Go_Fine.vi | Moves the slides exactly to the specified positions. A feedback loop to the encoders iteratively re-adjusts the position of the each slide with a precision of $10\ \mu\text{m}$. |
| Go_Null.vi | Moves the system to the reference position. |
| Go_Position.vi | Moves the slides by the specified number of steps. |
| Hardlimit1.vi | Move slide 1 to end-of-drive limit. |
| Hardlimit2.vi | Move slide 2 to end-of-drive limit. |
| Home1_2.vi | Perform reference run for both slides. The closest position without activated limit switch is set as reference position. |
| WDInitDrive95.vi | Initialises drive system and sets default values. This VI is working for MS Windows95 only. |

Table E.1:

List of the most important VIs of the *wedgedrive.llb* library controlling the linear stepping motor of the wedge drive system.

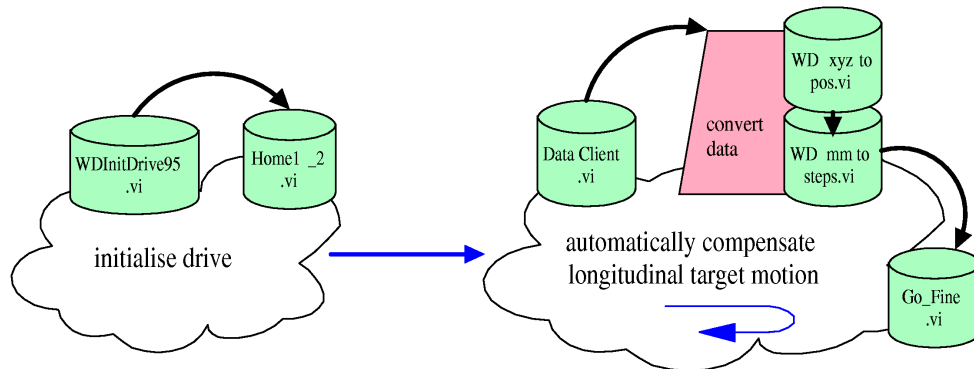


Figure E.1:

Process control for longitudinal target motion compensation. Before starting the motion compensation interface the wedge drive has to be manually initialised.

Appendix F

Time Behaviour of the Data Connection

The data connection between motion compensation (3D-OMC) and tracking system was designed in a flexible way, to allow communication with a wide variety of motion tracking systems. Without loss of generality, the following study of the time behaviour of this connection is based on a CAMAC interface for the measurement of the motion information, which can in general be replaced by any suitable interface. For the read-out procedure two different approaches exist: If the CAMAC controller is operated in the master mode, the data is collected simultaneously in the CAMAC crate and send sequentially to the 3D-OMC system. In this case, the data can only be transferred via ethernet¹. If the CAMAC controller is operated in slave mode, it can be connected to the master VME processor (E7) via VSB to differential bus interface (VSC)². In this case, the CAMAC bus is directly memory mapped. This eliminates the data transfer time, but the three coordinates are read-out sequentially. In summary, none of the two approaches yields absolutely time-consistent motion information. Either the three values are measured at the same time, but reach the 3D-OMC with a certain time lag, or the three displacement components are measured at slightly different time points, but the values are instantaneously available for compensation.

To estimate the time lag, the data transfer rate for both cases was investigated in a long-time test, taking and transmitting data every 10 ms for a total time of 600 s. This test included the data read-out connection between CAMAC (server) and the E7 (switch), which distributes the data to the scanning control and wedge drive system, as well as the data transfer from the E7 to the Win-PC (client), which controls the wedge drive. To investigate the time behaviour, the system time was recorded for every operation in each of the three subsystems. In the VSC case, the CAMAC controller (CVC) was operated as a slave for the E7 and the transmitted data string contained the system time of the E7 right before initialising the data

¹The current generation of CAMAC controllers used at GSI (CVC-90) supports only 10 MBit Ethernet connection in the master mode.

²designed at GSI by J. Hofmann.

read-out (server) and right before distributing the data in the 3D-OMC system (switch), as well as the time stamp of the Win-PC right after having received the data (client). For the investigation of the TCP/IP connection, the CVC was operated in master mode, running the same operating system as the E7 (LynxOS real-time operating system). In this case, the data string contained the same switch and client time information as in the VSC case, but the server time stamp was generated by the CVC, right before transmitting the data. In both cases, the Win-PC was connected to the E7 via ethernet.

Fig. F.1 shows the results of the performance test. From the time information of all three components, the time interval between two data sets (Δt) and the transfer time from one subsystem to the next is determined. In case of the VSC connection (upper part), a statistical analysis of the data (lower left graph) reveals an average time interval between two successive data sets of (16.9 ± 15.2) ms. The most likely time interval is in this case approximately 10 ms. As expected, the time interval distribution for the TCP/IP connection (lower part) is shifted to larger values, yielding an average interval of (25.8 ± 15.6) ms and a most likely time interval of approximately 20 ms. The upper, left graphs show in both cases a random distribution of the time intervals. Obviously, there is no systematic change in the read-out rate. The main difference between VSC and TCP/IP connection becomes apparent, when looking at the transfer time between the single 3D-OMC subsystems (right graph). While there is a significant, average transfer time between switch and server in case of the TCP/IP connection, this value is constantly zero with the VSC connection. In both cases, large spike-like structures occur in the transfer time distribution. In these spikes, the transfer time is elongated over 20-100 data sets. The delay results from a pronounced data traffic on the ethernet, slowing down the TCP/IP connection. In the TCP/IP connection case, the spikes occur in all three connections and coincide very well. With the VSC connection between switch and server, only one significant spike appears, which affects all three connections, all other, smaller spikes occur only in the two connections, involving the ethernet link. In contrast to the TCP/IP case, the large peak is about 400 ms delayed with respect to the two ethernet-based connections and is most likely a result of the slowed down switch. Such a feedback results from the heavy load of the E7 and occurs only for large delays in the ethernet connection. In all other cases, the resources of the E7 are large enough to provide a reliable VSC communication. Another striking feature in the transmission time data is the slope in the distribution for all connections involving the data client. This slope is, in first approximation, constant and, most likely, results from a small difference in time measurement between the two operating systems (Windows NT 4.0 on the data client and LynxOS on the switch and the data server). In the documentation of the Windows NT time service³, a deviation of 5.2×10^{-6} s is specified for a system obtaining its time

³<http://www.niceties.com/timeserv.htm>

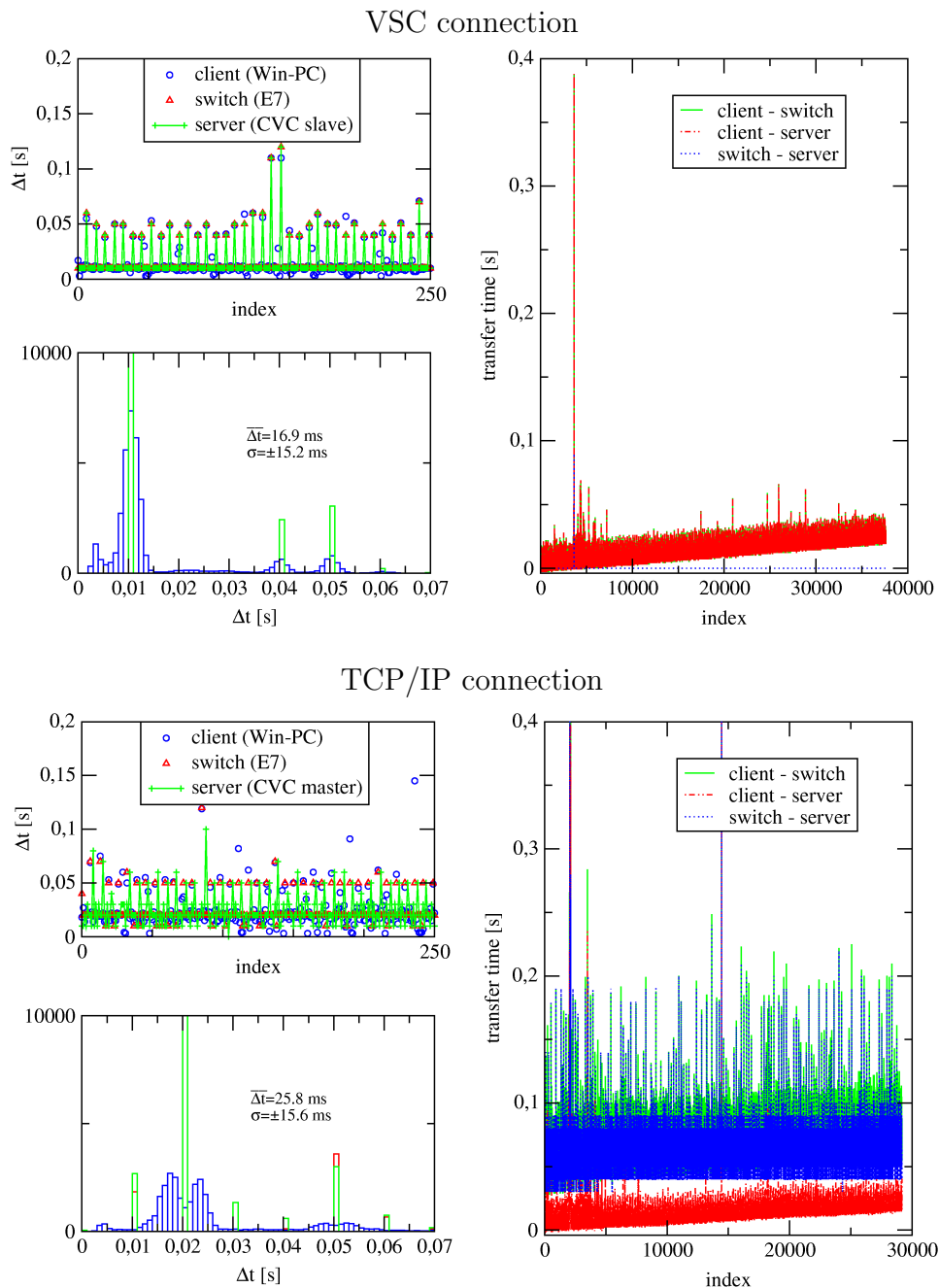


Figure F.1:

Investigation of the data transfer time lag for the 3D-OMC setup used in the feasibility study. The time interval (Δt) between two data sets and the data transfer time for each sub-connection are extracted from the system time of the data client (Win-PC, wedge drive), the data switch (E7, 3D-OMC master) and the data server (CVC CAMAC controller).

information from a non-network source. The time information in the performance test relies on network sources. According to the time service documentation, this leads to an even larger skew. The slope shown in fig. F.1 hints at a difference in the time measurement of $\pm(1.9 \times 10^{-5} \pm 0.2 \times 10^5)$ s. This difference has no effect on the practical operation of the 3D-OMC system, as the time information itself is not used.

Bibliography

- [Adl99] J. ADLER, M. MURPHY, S. CHANG, ET AL.: *Image-Guided Robotic Radiosurgery*, *Neurosurgery* **44**(6) (1999) 1299–1307
- [Ahl98] J. AHLWEDE, M. BOCK, T. BORTFELD, ET AL.: *T2-Measurements for Polymer Gel Based Three-Dimensional Dosimetry* (1998), URL http://www.dkfz.de/mrphys/geldosimetry/bang/ja_98.html, German Cancer Research Centre Heidelberg, Germany
- [Bai80] N. A. BAILY, R. A. HORN, T. D. KAMPP: *Fluoroscopic Visualization of Megavoltage Therapeutic X-ray Beams*, *Int. J. Radiat. Oncol. Biol. Phys.* **6**(7) (1980) 935–939
- [Bal95] J. M. BALTER, K. L. LAM, H. M. SANDLER, ET AL.: *Automated Localisation of the Prostate at the Time of Treatment using Implanted Radiopaque Markers: Technical Feasibility*, *Int. J. Radiat. Oncol. Biol. Phys.* **33**(5) (1995) 1281–1286
- [Bat00] B. BATHELT: *Filmdosimetrie in der Schwerionen-Tumorthherapie: 3-dimensionale Dosisverifikation in gemischten Teilchenstrahlenfeldern*, Ph.D. thesis, Universität GH Kassel (2000)
- [Bet30] H. BETHE: *Zur Theorie des Durchgangs schneller Korpuskularstrahlung durch Materie*, *Ann. Phys.* **5**(5) (1930) 325–400
- [Bet04] K. BETHGE, G. KRAFT, P. KREISLER, ET AL.: *Medical Applications of Nuclear Physics*, 1st ed. (Springer-Verlag, 2004), in press
- [Bla90] H. BLATTMANN, A. CORAY: *A Horizontal Proton Beam Line for the Development of a Scanning Technique*, *Radiother. Oncol.* **17** (1990) 17–20
- [Blo33] F. BLOCH: *Zur Bremsung rasch bewegter Teilchen beim Durchgang durch Materie*, *Ann. Phys.* **5**(16) (1933) 285–321
- [Bor94] T. BORTFELD, D. KAHLER, T.J.WALDRON, ET AL.: *X-ray Field Compensation with Multileaf Collimators*, *Int. J. Radiat. Oncol. Biol. Phys.* **28**(3) (1994) 723–730

- [Bor02] T. BORTFELD, K. JOKIVARSI, M. GOITEIN, ET AL.: *Effects of Intra-Fraction Motion on IMRT Dose Delivery: Statistical Analysis and Simulation*, Phys. Med. Biol. **47** (2002) 2203–2220
- [Bou01] L. G. BOUCHET, S. L. MEEKS, G. GOODCHILD, ET AL.: *Calibration of Three-Dimensional Ultrasound Images for Image-Guided Radiation Therapy*, Phys. Med. Biol. **46** (2001) 559–577
- [Bov97] F. J. BOVA, J. M. BUATTI, W. A. FRIEDMANN, ET AL.: *The University of Florida Frameless High-Precision Stereotactic Radiotherapy System*, Int. J. Radiat. Oncol. Biol. Phys. **38**(4) (1997) 875–882
- [Bra88] A. BRAHME: *Optimization of Stationary and Moving Beam Radiation Therapy Techniques*, Radiother. Oncol. **12** (1988) 129–140
- [Bro93] I. N. BRONSTEIN, K. A. SEMENDJAJEW, G. MUSIOL, ET AL.: *Taschenbuch der Mathematik*, 1st ed. (Verlag Harri Deutsch, 1993)
- [Bun00] BUNDESAMT FÜR STRAHLENSCHUTZ: *Strahlenthemen: Röntgendiagnostik – schädlich oder nützlich?*, BfS, Referat Presse- und Öffentlichkeitsarbeit, Postfach 100149, 38201 Salzgitter, Germany (2000)
- [Car01] S. K. CARLSON, C. E. BENDER, K. L. CLASSIC, ET AL.: *Benefits and Safety of CT Fluoroscopy in Interventional Radiologic Procedures*, Radiology **219** (2001) 515–520
- [Chu93] W. T. CHU, B. A. LUDEWIGT, T. R. RENNER: *Instrumentation for Treatment of Cancer Using Proton and Light-Ion Beams*, Accelerator and Fusion Research Division, LBL-33403 UC-406 preprint (1993)
- [Chu03] C. S. CHUI, E. YORKE, L. HONG: *The Effects of Intra-Fraction Organ Motion on the Delivery of Intensity-Modulated Field with a Multileaf Collimator*, Med. Phys. **30**(7) (2003) 1736–1746
- [Con92] D. J. CONVERY, M. E. ROSENBLOOM: *The Generation of Intensity-Modulated Fields for Conformal Radiotherapy by Dynamic Collimation*, Phys. Med. Biol. **36**(6) (1992) 1359–1374
- [Dav94] S. C. DAVIES, A. L. HILL, R. B. HOLMES, ET AL.: *Ultrasound Quantitation of Respiratory Organ Motion in the Upper Abdomen*, Br. J. Radiol. **67** (1994) 1096–1102
- [Deb98] J. DEBUS, M. WANNENMACHER, H. ZUR HAUSEN, ET AL.: *Proposal for a Dedicated Ion Beam Facility for Cancer Therapy*, GSI Darmstadt, Germany (1998)

- [DIN97] DIN EN 793: *Besondere Anforderungen für die Sicherheit von medizinischen Versorgungseinheiten*, Deutsches Institut für Normung e.V. und VDE Verband Deutscher Elektrotechniker e.V. (1997)
- [Don02] R. DONALDSON: *Osteology - Anatomical Orientations, Planes , Directions* (2002), URL <http://web.uvic.ca/anth/451/orientations.PDF>, ANTH451 Powerpoint lecture, University of Victoria, British Columbia, Canada
- [Ekb98] L. EKBERG, O. HOLMBERG, L. WITTGREN, ET AL.: *What Margins should be Added to the Clinical Target Volume in Radiotherapy Treatment Planning for Lung Cancer?*, *Radiother. Oncol.* **48** (1998) 71–77
- [Eng99] W. ENGHARDT, J. DEBUS, T. HABERER, ET AL.: *The Application of PET to Quality Assurance of Heavy-Ion Tumor Therapy*, *Strahlenther. Onkol.* **175**(suppl. II) (1999) 33–36
- [Gor84] J. C. GORE, Y. S. KANG, R. J. SCHULZ: *Measurement of Radiation Dose Distribution by Nuclear Magnetic Resonance (NMR) Imaging*, *Phys. Med. Biol.* **29** (1984) 1189–1197
- [GSI99] GSI DARMSTADT: *Bestrahlungssystem mit Intensitätsgesteuerter Tiefenmodulation zur volumenkonformen Bestrahlung von tiefliegenden Tumoren mit Protonen und leichten Ionen*, patent application, D 199 07 098.9, PCT/EP 00-01149 (1999)
- [GSI00] GSI DARMSTADT: *Präzisionsbestrahlung von bewegten Volumina mit dem Ionen-Rasterverfahren*, patent application, D 100 31 074.5, PCT/EP 01-07553 (2000)
- [GSI02] GSI DARMSTADT: *Optimierter Beschleunigerbetriebsmodus*, patent application, D 102 05 949.7, PCT/EP 02-14256 (2002)
- [Hab] T. HABERER: private communication
- [Hab93] T. HABERER, W. BECHER, D. SCHARDT, ET AL.: *Magnetic Scanning System for Heavy Ion Therapy*, *Nucl. Inst. & Meth. in Phys. Res.* **A330** (1993) 296–305
- [Hab94] T. HABERER: *Entwicklung eines magnetischen Strahlführungssystems zur tumorkonformen Strahlentherapie mit schweren geladenen Teilchen*, GSI Report **94-09** (1994)
- [Hag02] K. HAGIWARA, K. HIKASA, K. NAKAMURA, ET AL.: *Review of Particle Physics*, *Phys. Rev. D* **66** (2002) 010001+, URL <http://pdg.lbl.gov>

- [Han96] J. HANLEY, M. M. DEBOIS, A. RABEN, ET AL.: *Deep Inspiration Breath Hold Technique for Lung Tumors: The Potential Value of Target Immobilization and Reduced Lung Density in Dose Escalation*, Int. J. Radiat. Oncol. Biol. Phys. **36**(1) (1996) S188
- [Han99] J. HANLEY, M. M. DEBOIS, D. MAH, ET AL.: *Deep Inspiration Breath-Hold Technique for Lung Tumors: The Potential Value of Target Immobilization and Reduced Lung Density in Dose Escalation*, Int. J. Radiat. Oncol. Biol. Phys. **45**(3) (1999) 603–611
- [Har93] G. H. HARTMANN, B. BAUER-KIRPES, C. F. SERAGO, ET AL.: *Precision and Accuracy of Stereotactic Convergent Beam Irradiations from a Linear Accelerator*, Int. J. Radiat. Oncol. Biol. Phys. **28** (1993) 481–492
- [Hen82] R. M. HENKELMANN, K. MAH: *How important is Breathing in Radiation Therapy of the Thorax?*, Int. J. Radiat. Oncol. Biol. Phys. **8**(11) (1982) 2005–2010
- [Hen86] J. HENNING, A. NAUERH, H. FRIEDBURG: *RARE Imaging: A Fast Imaging Method for Clinical MR*, Magn. Reson. Med. **3** (1986) 823–833
- [Hes97] HESS. MINISTERIUM FÜR UMWELT, ENERGIE, JUGEND, FAMILIE UND GESUNDHEIT: *Genehmigungsbescheid [zum Betrieb der GSI Beschleunigeranlage zur Anwendung ionisierender Strahlen am Menschen in der medizinischen Forschung]* (1997)
- [ICR93] ICRU Report 50: *Prescribing, Recording and Reporting Photon Beam Therapy*, International Commission on Radiation Units and Measurements (1993)
- [ICR99] ICRU Report 62: *Prescribing, Recording and Reporting Photon Beam Therapy*, supplement to ICRU Report 50, International Commission on Radiation Units and Measurements (1999)
- [Jac97] C. JACOB: *Reichweite CT-Zahl Beziehung von Phantommaterialien*, Ph.D. thesis, Universität Heidelberg (1997)
- [Jäk01] O. JÄKEL, M. KRÄMER, C. KARGER, ET AL.: *Treatment Planning for Heavy Ion Radiotherapy: Clinical Implementation and Application*, Phys. Med. Biol. **46** (2001) 1101–1116
- [Jaf99] D. A. JAFFRAY, D. YAN, J. W. WONG: *Managing Geometric Uncertainty in Conformal Intensity-Modulated Radiation Therapy*, Semin. Radiat. Oncol. **9**(1) (1999) 4–19

- [Kea01] P. J. KEALL, V. R. KINI, S. S. VEDAM, ET AL.: *Motion Adaptive X-Ray Therapy: A Feasibility Study*, Phys. Med. Biol. **46** (2001) 1–10
- [Kir97] S. KIRSCH, H. U. BOKSBERGER, U. GREUTER, ET AL.: *Real-Time Tracking of Tumour Positions for Precision Irradiation*, in *Advances in Hadrontherapy* (U. Amaldi and B. Larsson and Y. Lemoigne, 1997), 269–274
- [Kle99] C. KLEIN: *Sonographie der Lunge und Analyse der Atmungsmechanik mittels Impuls-Oszilloresistometrie beim lungengesunden und pneumoniekranke Ferkel und Läufer Schwein*, Ph.D. thesis, Universität Leipzig (1999)
- [Kor92] H. W. KORIN, R. L. EHMAN, S. RIEDERER, ET AL.: *Respiratory Kinematics of the Upper Abdominal Organs: A Quantitative Study*, Magn. Reson. Med. **23** (1992) 172–178
- [Kra00] G. KRAFT: *Tumor Therapy with Heavy Charged Particles*, Prog. Part. Nucl. Phys. **45** (2000) S473–S544
- [Kra03] G. KRAFT: *Radiobiological Effects of Highly Charged Ions*, in *The Physics of Highly and Multiply Charged Ions* (edited by F. J. CURRELL) (Kluwer Academic Publisher, 2003)
- [Krä] M. KRÄMER: private communication
- [Krä00] M. KRÄMER, M. SCHOLZ: *Treatment Planning for Heavy Ion Radiotherapy: Calculation and Optimization of Biologically Effective Dose*, Phys. Med. Biol. **45** (2000) 3319–3330
- [Krä01] M. KRÄMER, O. JÄKEL, T. HABERER, ET AL.: *Treatment Planning for Heavy Ion Radiotherapy: Physical Beam Model and Dose Optimization*, J. Radiat. Res. **42** (2001) 39–46
- [Kub96] H. D. KUBO, B. C. HILL: *Respiration Gated Radiotherapy Treatment: A Technical Study*, Phys. Med. Biol. **41** (1996) 83–91
- [Lan01] K. M. LANGEN, D. T. L. JONES: *Organ Motion and its Management*, Int. J. Radiat. Oncol. Biol. Phys. **50**(1) (2001) 265–278
- [Lau86] T. LAUBENBERGER: *Technik der Medizinischen Radiologie*, 4th ed. (Deutscher Ärzte-Verlag, 1986)
- [Leo94] W. R. LEO: *Techniques for Nuclear and Particle Physics Experiments*, 2nd ed. (Springer-Verlag, 1994)

- [Li00] J. G. LI, L. XING: *Inverse Planning Incorporating Organ Motion*, Med. Phys. **27**(7) (2000) 1573–1578
- [Li04] Q. LI, S. O. GRÖZINGER, T. HABERER, ET AL.: *Online Compensation of Target Motion with Scanned Particle Beams: Simulations*, Phys. Med. Biol. in preparation (2004)
- [Lis92] J. LISTERUD, S. EINSTEIN, E. OUTWATER, ET AL.: *First Principles of Fast Spin Echo*, Magn. Reson. Quarterly **8** (1992) 199–244
- [Mac03] T. R. MACKIE, J. KAPATOES, K. RUCHALA, ET AL.: *Image Guidance for Precise Conformal Radiotherapy*, Int. J. Radiat. Oncol. Biol. Phys. **56**(1) (2003) 89–105
- [Mah00] D. MAH, J. HANLEY, K. E. ROSENZWEIG, ET AL.: *Technical Aspects of the Deep Inspiration Breath-Hold Technique in the Treatment of Thoracic Cancer*, Int. J. Radiat. Oncol. Biol. Phys. **48**(4) (2000) 1175–1185
- [Mar93] M. J. MARYANSKI, J. C. GORE, R. P. KENNAN, ET AL.: *NMR Relaxation Enhancement in Gels Polymerised and Cross-Linked by Ionizing Radiation: A New Approach to 3D Dosimetry by MRI*, Magn. Reson. Imaging **11** (1993) 253–258
- [Min00] S. MINOHARA, T. KANAI, M. ENDO, ET AL.: *Respiratory Gated Irradiation System for Heavy-Ion Radiotherapy*, Int. J. Radiat. Oncol. Biol. Phys. **47**(4) (2000) 1097–1103
- [Min02] S. MINOHARA, M. ENDO, T. KANAI, ET AL.: *Method to Estimate Uncertainties of the Range Calculation Associated with Patient Respiration*, in *Proceedings from PTCOGXXXVI* (Catania, Italy, 2002)
- [Mol48] G. MOLIERE: *Theorie der Streuung schneller geladener Teilchen II, Mehrfach- und Vielfachstreuung*, Z. Naturforsch. **3a** (1948) 78–97
- [Mor95] H. MORNEBURG: *Bildgebende Systeme für die medizinische Diagnostik*, 3rd ed. (Publicis MCD Verlag, 1995)
- [Oha89] K. OHARA, T. OKUMURA, M. AKISADA, ET AL.: *Irradiation Synchronized with Respiration Gate*, Int. J. Radiat. Oncol. Biol. Phys. **17**(4) (1989) 853–857
- [Oku95] T. OKUMURA, H. TSUJI, H. TSUJII: *Compensation of Target Motion*, in *Ion Beams in Tumor Therapy* (U. Linz, 1995), 308–315

- [Ped95] E. PEDRONI, R. BACHER, H. BLATTMANN, ET AL.: *The 200-MeV Proton Therapy Project at the Paul Scherer Institute: Conceptual Design and Practical Realization*, Med. Phys. **22** (1995) 37–53
- [Phi92] M. H. PHILLIPS, E. PEDRONI, H. BLATTMANN, ET AL.: *Effects of Respiratory Motion on Dose Uniformity with a Charged Particle Scanning Method*, Phys. Med. Biol. **37**(1) (1992) 223–234
- [Pöt98a] R. PÖTTER, T. AUBERGER, M. REGLER: *Med-AUSTRON - Ein Österreichisches Krebsforschungs- und Behandlungszentrum zur Hadronentherapie in Europa – Machbarkeitsstudie*, vol. 1 (1998)
- [Pöt98b] R. PÖTTER, T. AUBERGER, M. REGLER: *Med-AUSTRON - Ein Österreichisches Krebsforschungs- und Behandlungszentrum zur Hadronentherapie in Europa – Machbarkeitsstudie*, vol. 2 (1998)
- [Ram00] U. RAMM, U. WEBER, M. BOCK, ET AL.: *Three-Dimensional BANGTM Gel Dosimetry in Conformal Carbon Ion Therapy*, Phys. Med. Biol. **45** (2000) N95–N102
- [Reg02] M. REGLER, M. BENEDIKT, K. POLJANC: *Medical Accelerators for Hadrontherapy with Protons and Carbon Ions*, CERN Accelerator School, Hephy-PUB-757/02 (2002)
- [Rem00] P. REMEIJER, E. GEERLOF, L. PLOEGER, ET AL.: *3-D Portal Image Analysis in Clinical Practice: An Evaluation of 2-D and 3-D Analysis Techniques as Applied to 30 Prostate Cancer Patients*, Int. J. Radiat. Oncol. Biol. Phys. **46**(5) (2000) 1281–1290
- [Rie] E. RIETZEL: private communication
- [Rie03a] E. RIETZEL, G. CHEN, K. DOPPKE, ET AL.: *4D Computed Tomography for Treatment Planning*, Int. J. Radiat. Oncol. Biol. Phys. **57**(2) (2003) S232–233
- [Rie03b] E. RIETZEL, J. JACKSON, J. ADAMS, ET AL.: *The Impact of Organ Motion on Dose Distribution*, Med. Phys. **30**(6) (2003) 1428
- [Ros90] C. S. ROSS, D. H. HUSSEY, E. C. PENNINGTON, ET AL.: *Analysis of Movement of Intrathoracic Neoplasms using Ultrafast Computerized Tomography*, Int. J. Radiat. Oncol. Biol. Phys. **18**(3) (1990) 671–677
- [Sch93a] D. SCHARDT, H. STELZER, H. JUNK, ET AL.: *Bragg Curve Measurements with Ionisation Chambers*, GSI Scientific Report 1992 **GSI-93-1** (1993) 336

- [Sch93b] W. SCHLEGEL, O. PASTYR, T. BORTFELD, ET AL.: *Stereotactically Guided Fractionated Radiotherapy: Technical Aspects*, *Radiother. Oncol.* **29** (1993) 197–204
- [Sch93c] A. SCHWEIKARD, G. GLOSSER, M. BODDULURI, ET AL.: *Robotic Motion Compensation for Respiration Movement during Radiosurgery*, *J. Comput. Aided. Surg.* **A330** (1993) 296–305
- [Sch94] M. SCHOLZ, G. KRAFT: *Calculation of Heavy Ion Inactivation Probabilities Based on Track Structure, X-Ray Sensitivity and Target Size*, *Rad. Prot. Dosi.* **52** (1994) 29–33
- [Sch97] M. SCHOLZ, A. KELLERER, W. KRAFT-WEYRATHER, ET AL.: *Computation of Cell Survival in Heavy-Ion Beams for Therapy. The Model and its Approximation*, *Radiat. Environ. Biophys.* **36** (1997) 59–66
- [Sei00] P. G. SEILER, H. BLATTMANN, S. KIRSCH, ET AL.: *A Novel Tracking Technique for the Continuous Precise Measurement of Tumour Positions in Conformal Radiotherapy*, *Phys. Med. Biol.* **45** (2000) N103–N110
- [Shi00] H. SHIRATO, S. SHIMIZU, T. KUNIEDA, ET AL.: *Physical Aspects of a Real-Time Tumor-Tracking System for Gated Radiotherapy*, *Int. J. Radiat. Oncol. Biol. Phys.* **48**(4) (2000) 1187–1195
- [Sih98] L. SIHVER, D. SCHARDT, T. KANAI: *Depth-Dose Distribution of High-Energy Carbon, Oxygen and Neon Beams in Water*, *Jpn. J. Med. Phys.* **18**(1) (1998) 1–21
- [Spi00] P. SPILLER, D. BOEHNE, A. DOLINSKI, ET AL.: *Gantry Studies for the Proposed Heavy Ion Cancer Therapy Facility in Heidelberg*, Tech. rep., GSI Darmstadt (2000)
- [Spi01] B. SPIELBERGER, M. SCHOLZ, M. KRÄMER, ET AL.: *Experimental Investigations of the Response of Films to Heavy-Ion Irradiation*, *Phys. Med. Biol.* **46** (2001) 2889–2897
- [Spi02] B. SPIELBERGER, M. SCHOLZ, M. KRÄMER, ET AL.: *Calculation of the X-ray Film Response to Heavy Charged Particle Irradiation*, *Phys. Med. Biol.* **47** (2002) 4107–4120
- [Spi03a] B. SPIELBERGER, M. KRÄMER, G. KRAFT: *Three-dimensional Dose Verification with X-ray Films in Conformal Carbon Ion Therapy*, *Phys. Med. Biol.* **48** (2003) 497–505

- [Spi03b] B. SPIELBERGER, M. KRÄMER, M. SCHOLZ, ET AL.: *Three-dimensional Dose Verification in Complex Particle Radiation Fields based on X-ray Films*, Nucl. Inst. & Meth. in Phys. Res. **209** (2003) 277–282
- [Tad98] T. TADA, K. MINAKUCHI, T. FUJIOKA, ET AL.: *Lung Cancer: Intermittent Irradiation Synchronized with Respiratory Motion – Results of a Pilot Study*, Radiology **207** (1998) 779–783
- [US03] J. UUSI-SIMOLA, S. SAVOLAINEN, A. KANGASMÄKI, ET AL.: *Study of the Relative Dose-Response of BANG-3TM Polymer Gel Dosimeters in Epithermal Neutron Irradiation*, Phys. Med. Biol. **48** (2003) 2895–2906
- [Web93] S. WEBB: *The Physics of Three-Dimensional Radiation Therapy*, 1st ed. (IOP Publishing Ltd., 1993)
- [Web96] U. WEBER: *Volumenkonforme Bestrahlung mit Kohlenstoff-Ionen zur Vorbereitung einer Strahlentherapie*, Ph.D. thesis, Universität GH Kassel (1996)
- [Web00] U. WEBER, W. BECHER, G. KRAFT: *Depth Scanning for a Conformal Ion Beam Treatment of Deep Seated Tumours*, Phys. Med. Biol. **45** (2000) 3627–3641
- [Wil46] R. R. WILSON: *Radiological Use of Fast Protons*, Radiology **47** (1946) 487–491
- [Won97] J. W. WONG, M. B. SHARPE, D. A. JAFFRAY: *The Use of Active Breathing Control (ABC) to Minimize Breathing Motion in Conformal Therapy*, in *Proceedings of the 12th International Conference on the Use of Computers in Radiation Therapy* (edited by D. LEAVITT, G. STARKSCHALL) (1997), 220–222
- [Won99] J. W. WONG, M. B. SHARPE, D. A. JAFFRAY, ET AL.: *The Use of Active Breathing Control (ABC) to Reduce Margin for Breathing Motion*, Int. J. Radiat. Oncol. Biol. Phys. **44** (1999) 911–919
- [Yu98] C. X. YU, D. A. JAFFRAY, J. W. WONG: *The Effects of Intra-Fractional Organ Motion on the Delivery of Dynamic Intensity Modulation*, Phys. Med. Biol. **43** (1998) 91–104

Acknowledgements

Having completed this thesis I want to take the opportunity to express my gratitude to all people involved in this work.

First of all, I am deeply grateful to Prof. Dr. Gerhard Kraft for giving me the opportunity to work on this exciting topic, for his invaluable advice, his permanent support, his limitless interest in the progress of the project, and the many inspiring discussions. Simply, for everything!

I want to acknowledge Prof. Dr. D.H.H. Hoffmann for his expertise and interest in my work.

I am particularly thankful to Dr. Thomas Haberer for his support, always finding time for fruitful discussions and repeatedly "leaping in the ring" to arrange everything I needed in the course of this project.

I am deeply indebted to Dr. Eike Rietzel, who was always a great help, source of ideas, an immeasurably important conversational partner and improved the quality of this thesis with his detailed comments, to Dr. Qiang Li for his assistance in programming the simulation environment and his continuous interest in the project even after having left GSI, as well as to Christoph Bert and Wolfgang Becher for their perfect participation in this project.

I especially appreciate the great help from Dr. Dieter Schardt, Dr. Peter Heeg and Dr. Michael Krämer, which I could ask everything about experiments, CaveM, medical physics and programming, respectively, and which always had a helping hand. I want to thank Dr. Belinda Spielberger and Dr. Uli Weber for their immense support even after having left GSI.

I want to thank Elko Schubert, Günter Lenz, Ingo Ragaller and David Lotz for their engineering and mechanical support, Dr. Holger Brand, who introduced me into LabView, Dr. Wolfgang Ott for his support in adapting the therapy control software and Dr. Klaus Poppensieker, whom I might have driven crazy with my ideas and requests for dedicated electronics. Klaus I'm not finished, yet!

It was a pleasure to collaborate with Dr. Achim Bankamp from the DKFZ in Heidelberg, Dr. Ulla Ramm and Jussi Moog, both from the university hospital in

Frankfurt, who supported me in the BANGTM gel experiments. Thanks a lot for your help!

I want to acknowledge the whole biophysics group for the wonderful, familial atmosphere; you were the reason for me enjoying to go to work every morning. A very special thank you goes to Konstanze Gunzert-Marx for the help in all circumstances, to Petra Sander for the catering, whenever I stayed longer at GSI or was busy writing this thesis – Petra, your sweets calendar saved lives –, to Dr. Stephanie Berger and Dr. Thorsten Grösser, from which I learned a lot about Biology, and to all my (former) room-mates Dr. Jakob Naumann, Marcus Winter, Paulo Crespo, Dr. Qiang Li and Wolfgang Becher for the great time.

Last but not least, I am very grateful for the backup I received from my family. I want to thank my parents for all the support and encouragement they have given me throughout my education. And above all, my profoundest thanks to my wonderful wife Anette for all her understanding, care and invaluable help not only in discussing and proofreading this thesis. Anette this work is dedicated to you.